

AHEAD Workpackage 8 JRA X-ray Optics

Deliverable D8.3 - D37

Design report on the collimated X-ray beam

Written by	Carlo Pelliciani (MPE) Benedikt Menz (MPE)	
Checked by	Vadim Burwitz (MPE)	
Distribution List	AHEAD Management Team Vadim Burwitz WP8.0, WP8.1, WP8.3 Dick Willingale WP8.1 Rene Hudec WP8.1 Daniele Spiga WP8.1, WP8.2	
Distribution Date	Draft Version Final Version	Nov 29, 2016 Dec 07, 2016



Contents

1	Motivation	3
2	Introduction	3
3	X-ray optics	4
3.1	Principles for X-ray optics	4
3.2	X-ray telescope optics	5
3.2.1	Concepts for X-ray telescopes	6
3.2.2	Wolter type 1 optics	6
4	X-ray collimator	8
4.1	Limitation using a finite source distance	9
4.2	An X-ray collimator for ATHENA	12
5	Zone Plate Optics	13
5.1	Basic formulas for the ideal zone plate ZP	14
5.2	Diffraction Efficiencies	16
5.2.1	The diffraction efficiency - theoretical limits	16
5.2.2	The diffraction efficiency - calculations for the ZPC	17
5.3	Angular resolution	21
5.3.1	Theoretical basis - the general OPD	21
5.3.2	Aberrations - the Quantitative Description	23
5.4	Avoiding background: geometric solutions	25
5.4.1	The diffracted wavefront - using apertures to select the collimated beam	25
5.4.2	Imaging multiple point sources - angular distance in the detector plane	26
6	Design of the Zone Plate Collimator	27
6.1	Design of the ZP	29
6.2	Fabrication process of the ZPC	29
7	Summary	32

1. Motivation

The science derived by measurements of astrophysical sources can only be as good as the calibration of the optics. One question of particular interest in the calibration of X-ray imaging optics for space telescopes concerns the characteristics of the point spread function (PSF) in orbit and the focal length for an infinite source distance. With ground based facilities, the PSF measurement of an X-ray telescope is limited by the finite source distance. In order to measure the PSF similar to that in space, a collimated X-ray beam is required.

In this document we investigate the feasibility of fabricating a large area transmission X-ray zone plate (ZP) as a collimator for testing X-ray optics. A ZP is basically a rotationally symmetric grating with radially increasing line density that changes the X-ray light path by diffraction. The efficiency of X-ray ZPs is highly dependent on material, energy, and geometry. Therefore, we compared various materials to determine their capacity to operate a ZP at an energy of 1.49 keV (Al- K_{α} emission line) which is typically used to characterize the PSF of X-ray telescope optics. X-ray ZPs are generally used as focusing devices in e.g. X-ray microscopy and using a ZP as a collimator is a new application. A geometric design for a large area X-ray zone plate collimator (ZPC), which is based on theoretical calculations is presented.

2. Introduction

Astronomical observations in the X-ray wavelength band have been essential to deepen the knowledge of astrophysical processes. Recently, the ESA has started a phase A study of the next generation X-ray observatory i.e. ATHENA [22], a large scale mission that will transform our understanding of the hot and the energetic universe. In order to accomplish the scientific goals, the optics of ATHENA need to meet demanding requirements, in particular, a large effective area ($A_{eff} = 2 \text{ m}^2$ at 1 keV) and a high angular resolution measured as HEW (HEW = $5''$).

This unique combination of large area and high angular resolution provides the ground breaking leap in sensitivity required to achieve the science goals and sets ATHENA apart from all previous X-ray telescopes. This is illustrated in Fig. 1.1. If the area at 1 keV is less than $\sim 0.1 \text{ m}^2$ then most cosmic sources are photon starved and the observation times required are prohibitively long. If the HEW is greater than ~ 10 arc sec source confusion in deep exposures is unacceptable. ATHENA is in the Golden Quadrant which provides very high sensitivity and minimal source confusion.

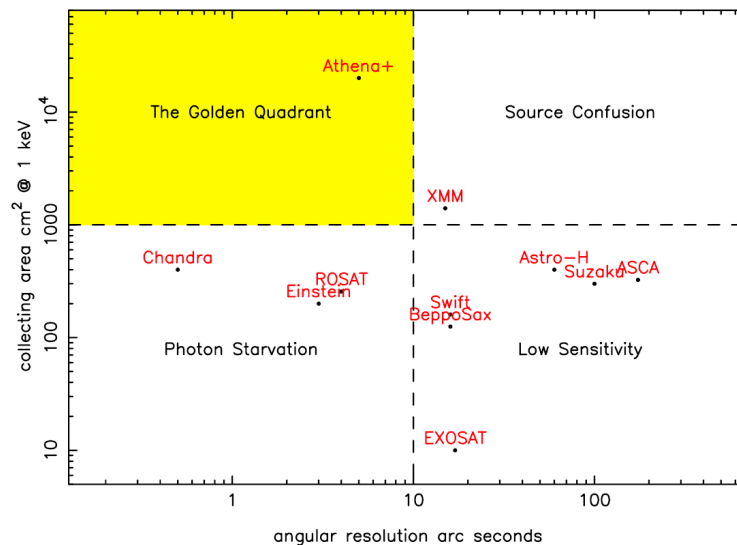


Figure 1: The performance of X-ray telescope modules. (Taken from Ref. [38] Fig.1)

For the scientific success of the ATHENA mission, the realization of suitable X-ray optics is of paramount importance. Previous optics concepts (section 3) are so far not able to combine the large effective area with a high

angular resolution. In order to realize ATHENA, a new concept for the optics has been studied and investigated. Proposed are segmented mirror modules in the Wolter 1 configuration using Silicon Pore Optics (SPO) technology [38, 37].

Essential for the development is the measurement of the angular resolution and the effective area. The optical performance of a space-based X-ray telescope can be determined before launch by using a set-up as close as possible to the in-orbit configuration. This is accomplished by locating an X-ray source as far away as possible from the telescope prototype to approximate a collimated incident beam. X-ray test facilities, such as NASA beam-line at GSFC (600 m beam path length) and the PANTER X-ray test facility, Germany (134 m beam path length) of the MPE, have been built in order to characterize the optics of X-ray telescopes. Those facilities provide a beam path length which is long compared to the focal length f of the telescope optics (e.g. $f = 12$ m for ATHENA). However, these beam path lengths are short compared to the distance to astrophysical X-ray sources.

Assuming that an astrophysical X-ray source is at an infinite distance, the spherical wavefronts of this astrophysical source become plane waves. Hence, the beam of an astrophysical X-ray source is parallel. In order to get a parallel X-ray beam at a ground based facility a dedicated collimating device has been studied.

In present document we report:

- definition of the Zone Plate X-ray collimator (ZPC);
- set-up improvements necessary to measure the performance of an ATHENA type optic;
- collimator requirements;
- theory and parameters investigation of efficiency and angular resolution;
- performance limitations due to optical aberrations;
- geometrical solution in order to minimize contribution caused by higher diffraction orders.

3. X-ray optics

There is a wide variety of X-ray optics that all have a common goal: to change the direction of incoming X-rays by a well defined value. X-ray optics differ considerably from optics in the visible bandpass. This is due to the properties of the refractive index n . For X-rays, the refractive index n deviates only slightly from unity and has usually a real part smaller than 1. Therefore, it is normally defined as

$$n = 1 - \delta - i\beta \quad (1)$$

with the index decrement δ and the absorption coefficient β .

All types of optics can be classified by the physical effect they make use of. These effects, investigated theoretically in Sect. 3.1, are refraction, reflection, and diffraction. All three physical effects can be utilized to build X-ray optics for various applications. Two fundamental applications of these X-ray optics are discussed: X-ray metrology and X-ray astronomy.

The first application, the realization of an X-ray optic for metrology, is the essential part of this report. As already mentioned in the introduction, this work discusses how an X-ray optic can be used as a collimator for the purposes of characterizing astronomical X-ray optics. In the following section, the basic principles of an optical system for an X-ray telescope are reviewed. Various practical concepts for X-ray telescope optics are presented in Sect. 3.2.1. The most common approach, the Wolter type 1 optic, is then discussed in more detail in Sect. 3.2.2.

3.1. Principles for X-ray optics

In the present section we report the basic concepts of X-ray optics, specifically how they can be realized to work efficiently in the 0.1 keV to 10 keV range. Since in this energy range absorption by the atmosphere is high, vacuum is in general required as a surrounding medium.

Refractive optics (Fig. 2a): Refraction occurs, when an electromagnetic wave passes from one medium into another with a different index of refraction. Hence, for a focusing refractive optic the required shape of the lens is defined by the index decrement δ and can be calculated using Snell's law. As δ is typically in a range of 10^{-2} to 10^{-6} in the X-ray regime, the refraction index n is less than but very close to one. With $n_{lens} < 1$ and the refraction index of the

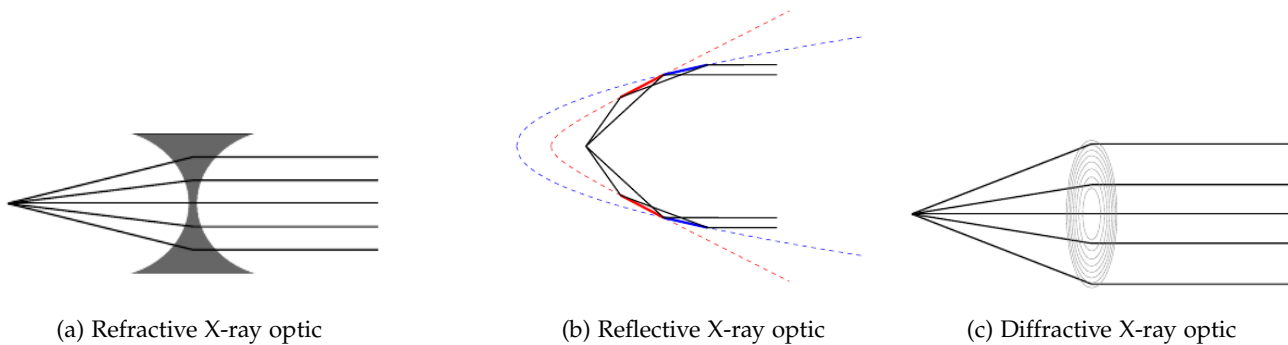


Figure 2: Schematics of X-ray lenses.

surrounding medium equal to unity ($n_{vac} = 1$), the lens surface must be concave. Schematically, such a lens is shown in Fig. 2a. X-ray refractive lenses are rarely used due to the low efficiencies of these optics. Due to the concave surface, the path length through the medium increases with the aperture radius and hence, the X-ray absorption increases. However, the feasibility of a refractive X-ray lens was demonstrated by use of a compound refractive lens [31] using low Z materials and focusing the X-rays by a series of holes in the material.

Reflective optics (Fig. 2b): Specular reflection is the mirror-like reflection of an electromagnetic wave from a surface. The direction of the incoming and the direction of the outgoing light have the same angle with respect to the surface normal. In the X-ray band high reflectivities from single surfaces are only obtained at grazing angles of incidence.¹ This is because the refractive index of the reflecting medium is very close to and slightly less than that of the surrounding medium (vacuum). This low optical contrast results in a correspondingly low graze angle for total (external) reflection. By using curved surfaces, it is possible to create focusing *reflection optics*. A concave spherical mirror can be used to form a good image of a point source on the optical axis. This is no longer the case when the source is moved away from the optical axis, because the aberrations become severe for grazing incidence angles. In order to obtain a two-dimensional image, compound systems in which the radiation is reflected at grazing incidence from an even number of curved surfaces are used. Two common geometries of such reflecting optics exist. These are generally known as Kirkpatrick-Baez and Wolter optics. In Fig. 2b, a Wolter type 1 is shown as an example of a reflective optic. Wolter optics, discussed in Sect. 3.2.2, are most commonly used to build X-ray telescopes.

Diffractive optics (Fig. 2c): Diffraction is the change in the propagation of light, when a wave encounters an obstacle. While diffraction technically occurs whenever propagating waves encounter an obstacle, its effects are generally most pronounced for waves whose wavelength is roughly comparable to the dimensions of the diffracting object. Hence, X-ray diffractive optics will have components with small structures. A typical geometry for a diffractive optic is a ZP, schematically shown in Fig. 2c. Other concepts, such as photon sieves [15] or interferometers [5], may provide even higher angular resolutions than a ZP. ZP and their focusing properties are a major part of this work. Therefore, the concept of a ZP and its aberrations are discussed in more detail in section 5.

3.2. X-ray telescope optics

X-ray optics for astronomy differ considerably from those X-ray optics used e.g. at synchrotron or at free electron laser laboratories. The reason for this is that in the range from 0.1 keV to 10 keV the absorption by the atmosphere is high. Due to the high absorption by the Earth's atmosphere, experiments for X-ray astronomy must be located in

¹ Multi layer mirrors might enable normal incidence reflection optics. The successful usage of such optics has been shown for the extreme ultra violet regime [20]. For the X-ray regime multi layer coatings are mainly discussed, to improve the reflectivity of grazing incidence optics.

space. This means that one is dependent on satellites to do X-ray astronomy². Since the weight is a significant cost factor for satellite experiments, the optics for X-ray telescopes must be as light as possible.

The principles described in Sect. 3.1 are further examined focusing on the application in the field of X-ray telescope optics. The key parameters that describe a telescope optic are the angular resolution and the effective area. Theoretically, each principle discussed in Sect. 3.1 allows diffraction-limited imaging. In reality, and especially due to the requirement that the optics must be lightweight, the angular resolution is limited primarily by the fabrication process. In Sect. 3.2.1 the advantages and disadvantages of different types of optics are discussed. So far most X-ray telescopes use the concept of a Wolter type 1 optic. The design and the realization of an X-ray telescope, which uses a Wolter type 1 optic, is discussed in detail in Sect. 3.2.2.

3.2.1. Concepts for X-ray telescopes

Purely refractive optics are unsuitable for X-ray telescopes due to their concave surface. The larger the aperture, the thicker the lens becomes towards the edge. Due to absorption of X-rays in matter, the efficiency decreases with increasing thickness. Consequently, pure refractive optics cannot be used in X-ray astronomy because a larger aperture does not result in a higher collecting area.

As a pure diffractive optic, a ZP is discussed as a telescope optic. A ZP can provide a high efficiency combined with an excellent angular resolution. However, both are valid for only one wavelength. It is possible to analyze coronal active regions of the sun with a ZP at the O VII line ($2.16 \text{ nm} = 0.574 \text{ keV}$) [17]. For all other wavelengths the point image is de-focused and the efficiency reduced. These effects are discussed in detail in section 5. Consequently, X-ray telescopes with only a ZP as optic are not suitable for astronomy due to chromatic effects.

It has been proposed theoretically to use interferometers or a combination of diffractive-refractive optics. The theoretical possibilities that are given by such optics are very promising. However, they have not been realized because the necessary focal lengths are in the range of kilometers to hundreds of kilometers. Such focal lengths can only be achieved with formation flight, which is a considerable technical effort.

For X-ray astronomy, specular reflection is mostly used when fabricating optics for an imaging telescope. Pure reflective optics have the advantage that they are theoretically achromatic. The physical effect of total external reflection enables also high efficiencies in the X-ray regime. By exploiting these physical effects, H. Wolter [42] proposed a geometry to build an imaging X-ray optic. Originally intended for X-ray microscopy, the so called Wolter optics are used today primarily in X-ray astronomy. In the following, the principle and manufacturing processes are examined in more detail.

3.2.2. Wolter type 1 optics

The principle of Wolter type 1 optics is shown schematically in Fig. 3. The X-rays are reflected twice: first from an inner parabolic surface and then from an inner hyperbolic surface.³ The theory of Wolter type 1 optics, especially concerning the resolution and off axis aberrations, is widely discussed in literature. Therefore, the presentation here is brief and given without proof. Further details and more rigorous calculations can be found in Ref. [34, 36, 39, 27, 26].

To increase the collecting area, several mirror shells can be nested con-focally, as shown in Fig. 3. The optimization of the off axis performance of such a nested mirror system has been discussed [29, 42]. The so called Wolter-Schwarzschild configuration provides a possibility to eliminate coma errors.

The top view and a cross section of the nested mirror system, as planned for ATHENA, are shown schematically in Fig. 4a and Fig. 4b respectively. To provide the collecting area of $\sim 2 \text{ m}^2$ at 1 keV required for ATHENA the optic modules must be densely populated. The aperture diameter of $\sim 3 \text{ m}$ is limited by the spacecraft. In order to increase the off-axis performance, the mirror modules are integrated across a spherical principal plane in the Wolter-Schwarzschild configuration.

One of the biggest challenges for ATHENA is the angular resolution of the optics, which is required to be 5 arc sec. The resolution of a lightweight X-ray optic is in general limited by manufacturing and not by theory [45]. Effects, such as surface roughness, figure errors, mounting, and the alignment of the individual mirror modules, reduce

² Besides satellites, balloon or rocket experiments are also possible. However, the large past missions as the ROSAT, current missions, as the XMM-Newton and the CHANDRA, and upcoming observatories as ATHENA are satellite-borne telescopes.

³ In Wolter type 2 and type 3 optics, the X-rays are reflected at the outer surface of the paraboloid and on a second inner surface.

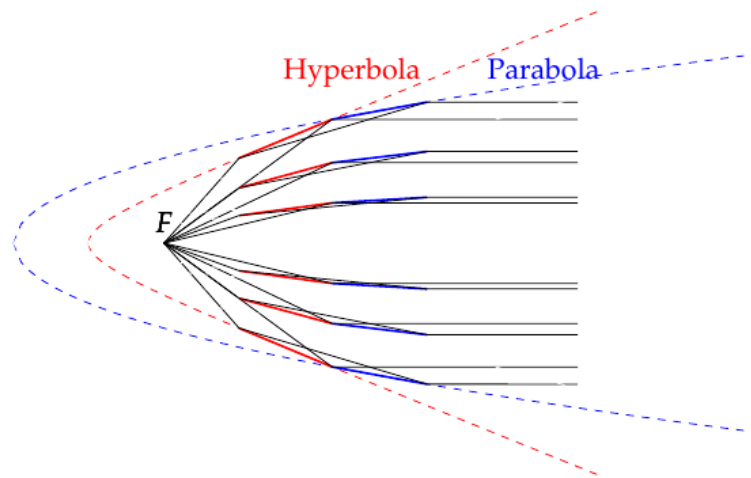


Figure 3: Schematic of a Wolter type 1 optic. The X-rays are reflected twice. First from an inner parabolic surface and then from an inner hyperbolic surface. To increase the collecting area mirror shells are nested con-focally.

the angular resolution. In order to avoid, or at least reduce the influence of these effects, different manufacturing techniques are used and optimized to fabricate X-ray optics. A brief summary, without claim of completeness, presents in the following the manufacturing processes commonly used to fabricate X-ray telescope optics.

The optics of most existing X-ray observatories are based on the concept of monolithic mirrors. Polished glass mirrors, as shown in Fig. 5a, have been used for ROSAT (HEW < 5 arc sec and $A_{eff} = 83 \text{ cm}^2$ at 1 keV) [33]) and CHANDRA (HEW = 0.5 arc sec and $A_{eff} = 400 \text{ cm}^2$ at 1 keV) [35]. This technology provides the best-ever angular resolution. This angular resolution comes at the expense of the collecting area. Since the glass mirror needs a certain thickness of several centimeters, such optics cannot be fabricated lightweight.

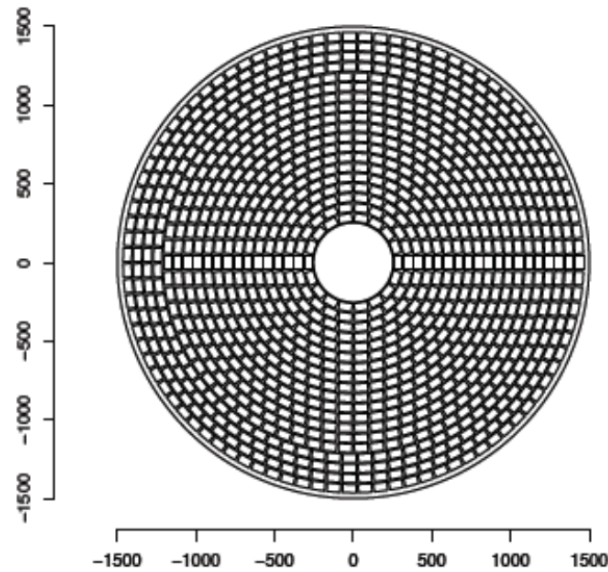
Nickel electro-formed mirror shells, as shown in Fig. 5b, with a thickness of millimeters, as used for XMM-Newton (HEW ≈ 14 arc sec and $A_{eff} = 4400 \text{ cm}^2$ at 1.5 keV) [14] and the optics for the eROSITA mission (HEW ≈ 16 arc sec and $A_{eff} = 2150 \text{ cm}^2$ at 1.5 keV) [24]) have two advantages. They are thin, and hence lightweight, and they can be replicated. E.g. for XMM-Newton three flight modules have been replicated and for eROSITA seven. Hence, they provide a large collecting area. However, nickel electro-formed mirror shells have a moderate angular resolution.

The scientific success of X-ray observatories based on monolithic shells is huge. However, to enable observations in the Golden Quadrant, as shown in Fig. 1, a new concept seems to be necessary. To obtain a good angular resolution with a lightweight optic for the upcoming X-ray observatory ATHENA, a modular concept is proposed. The idea is to fabricate mirror modules with a resolution better than 5 arc sec. By replicating these modules, the large collecting area required for ATHENA will be achieved.

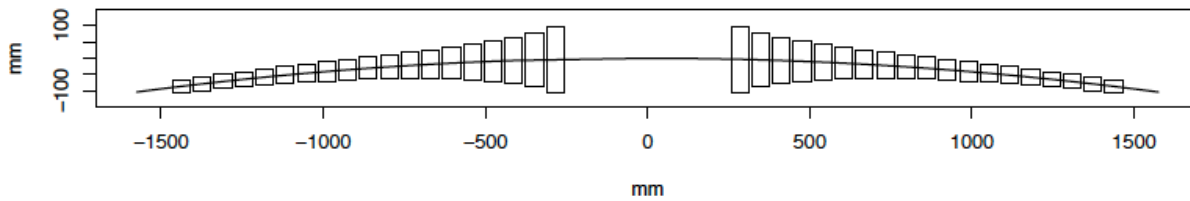
A modular optic concept for an X-ray telescope has been successfully realized for NuSTAR [11]. This mission, especially optimized to have a large collecting area at high energies ranging from 10 keV to 100 keV, uses SGO technology. This mission demonstrates the feasibility of a telescope with an optic based on segmented mirror modules. However, the angular resolution of the mirror modules, which is 60 arc sec, would not fulfill the angular resolution requirements for ATHENA.

The angular resolution for each ATHENA mirror module is required to be better than 5 arc sec, which is an order of magnitude better compared to the resolution of the NuSTAR optics. Two fabrication technologies have been investigated for ATHENA to manufacture such lightweight optic modules. One is the SGO technology [40, 23, 6], the slumping of thin glass foils as for NuSTAR (see Fig. 5c). The other is the bonding of curved silicon wafers to the SPO [38, 37], as shown in Fig. 5d. Both concepts have achieved great progresses so far. However, as the required resolution of 5 arc sec has not yet been achieved, both concepts are still in the development phase.

The project of this report, a large area X-ray collimator, also contributes to the optics development. The requirements of the X-ray collimator, discussed in detail in the next chapter, depend on the optic design of ATHENA. The angular resolution and the aperture of a mirror module are especially important for the collimator design. The angular resolution of a mirror module is required to be better than 5 arc sec. The aperture of a mirror module is



(a) Top view of the mirror aperture. The SPO modules create a mirror with an aperture radius of 1.5 m. Modules are arranged in rings to populate the aperture. Image taken from Ref. [38] Fig. 5.



(b) Cross-section of the mirror aperture. The SPO modules are integrated across a spherical principal plane in the Wolter-Schwarzschild configuration. Image taken from Ref. [38] Fig. 14.

Figure 4: Schematic of the ATHENA X-ray telescope optics. Each square indicates a SPO module as shown in Fig. 5d.

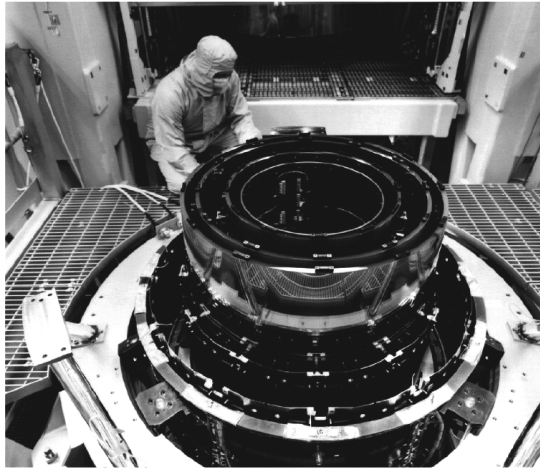
measured by its radial and azimuthal size. Currently, the individual mirror modules for ATHENA are planned with a radial height of 2.6425 cm, which is the stack height of a SPO. The azimuthal size of the module depends on the distance to the optical axis and ranges from 3.0 cm for the inner mirror radii to 10.0 cm for the outer mirror radii. Thus, the aperture is up to $\approx 3 \text{ cm} \times 10 \text{ cm}$.

4. X-ray collimator

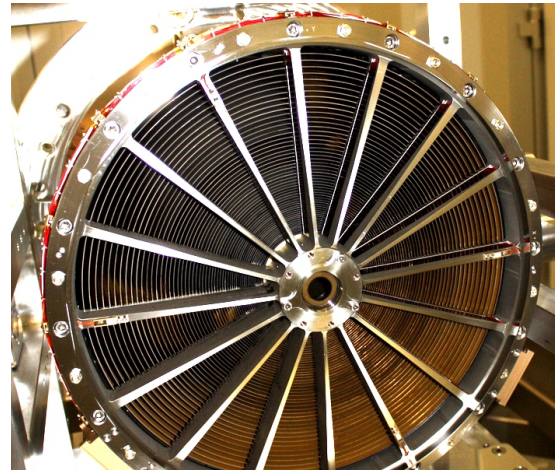
A collimator is an optical device that produces a non-divergent beam of light. A perfectly collimated beam, with no divergence, cannot be created due to diffraction. However, light can be approximately collimated by a number of processes. Two physical principles are shown in Fig. 6.

For particle beams, X-rays, and gamma rays usually the concept shown in Fig. 6a is applied. Such an *absorbing collimator* filters a stream of rays so that only those traveling parallel to a specified direction are allowed through. It is usually used for high energetic radiation, as it is challenging to focus radiation with such short wavelengths into an image by the use of lenses as it is routine with electromagnetic radiation at optical or near-optical wavelengths.

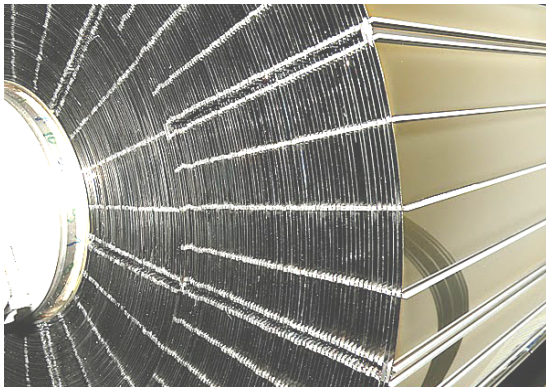
In the optical wavelength regime a collimator usually is realized by using a lens, as shown in Fig. 6b. Such a *lens collimator* parallelizes the light by changing the propagation direction of the light. All types of lenses are classified by their underlying physical effect, which have been theoretically discussed in Sect. 3.1. The effects, to change the



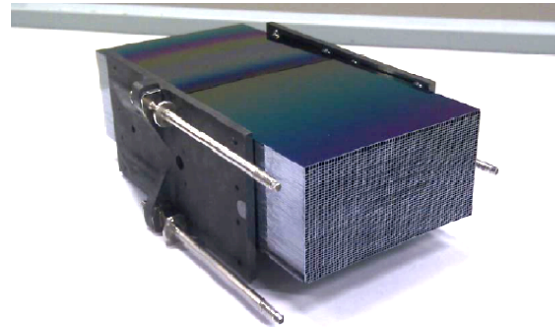
(a) CHANDRA HRMA. Four high polished glass mirror modules make up the telescope optic. Image taken from Ref. [35] Fig. 2.



(b) eROSITA mirror module. The 54 mirror shells are made of nickel and each shell is produced by electroforming from a highly polished negative form, a mandrel. In total eROSITA is built up from seven such replicated X-ray mirror modules.



(c) An end view of the NuSTAR optics. The telescope is built up by combining mirror modules, made of thin glass sheets. Image taken from Ref. [8] Fig.2.



(d) A SPO mirror module as planned for ATHENA. The observatory will combine hundreds of such mirror modules, arranged as shown in Fig. 4. Image taken from Ref. [38] Fig. 4

Figure 5: Realized X-ray telescope optics.

path of light, are refraction, reflection, and diffraction. Both collimator types can be used to build large area X-ray collimators. While the *absorbing collimator* can be set up by geometric consideration, the *lens collimator* requires a detailed consideration of the underlying physical processes.

The motivation to build an X-ray collimator is that the PSF of X-ray telescope optics can be measured realistically. To what extent the current measurements suffer from approximations is examined in detail in Sect. 4.1.

In order to build the collimator its requirements have to be defined. The optic concept for the upcoming X-ray observatory ATHENA, which has been discussed in detail in Sect. 3.2, defines these requirements. In order to fulfill these requirements different optical concepts in Sect. 4.2 are studied.

4.1. Limitation using a finite source distance

As discussed in Sect. 3.2, the optics for the next big X-ray observatory ATHENA are still under development. Essential for improving the angular resolution is that the PSF of the mirror modules is accurately measured. A number of measuring methods are used in order to obtain the results.

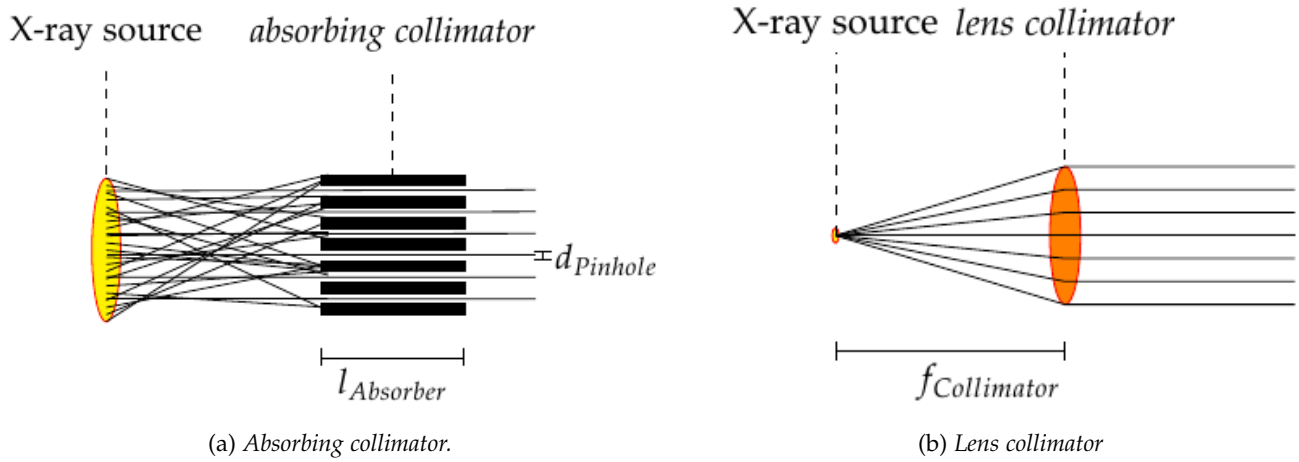


Figure 6: Schematics of different collimator types. For particle beams, X-rays, and gamma rays usually *absorbing collimators* are used. For the optical wavelength regime a collimator usually is realized by a lens.

One possibility is based on surface measurements of the mirror shells, e.g. using interferometers. Using these data the mirror surface can be modeled and the PSF can be determined by ray tracing, as e.g. in Sect. 5.4. This indirect method has the particular advantage that e.g. manufacturing influences can be measured quickly and directly. However, the PSF is only derived indirect and hence is approximated.

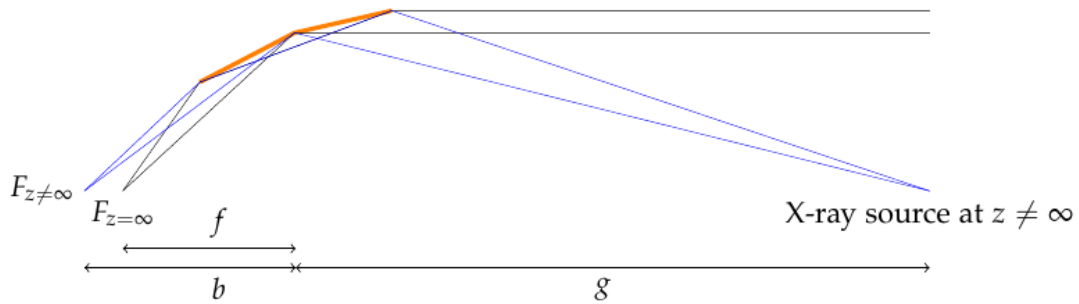


Figure 7: Divergent (blue) and parallel (black) illumination of a Wolter typ 1 optic with a focal length f . At a finite source distance g the image distance b is larger than f .

The only direct method of measuring the PSF is by imaging an X-ray point source as in orbit, schematically shown in Fig. 7. In order to simulate an orbit like point source facilities as PANTER are used. Such facilities provide an object distance $g = 122$ m which is long compared to the focal length f of the mirror (e.g. for ATHENA $f = 12$ m). However, this object distance is short compared to the one an astrophysical source has. The approximations which are caused by a finite source distance are, therefore, considered below. This is discussed for an ATHENA like Wolter type 1 SPO.

Schematically, the difference between finite (blue) and infinite source distance (black) is shown in Fig. 7. While in orbit, the image distance b equals the focal length f , a finite object distance g on ground increases the image distance. This effect leads for ATHENA to an image distance of $b = 13.3$ m. This effect can be calculated using the thin lens equation (2):

$$\frac{1}{b} = \frac{1}{f} - \frac{1}{g} \quad (2)$$

A divergent beam changes the illumination of a Wolter type 1 optic. For simplicity the effects are discussed for the on-axis case. First, the ideal case with parallel X-ray illumination is considered. This case is shown schematically

in Fig. 8. The parabola, at an angle α relative to the optical axis, reflects the X-rays by 2α . The once reflected light is then reflected a second time by the hyperbola. It is focused at an angle of 4α relative to the incoming beam.

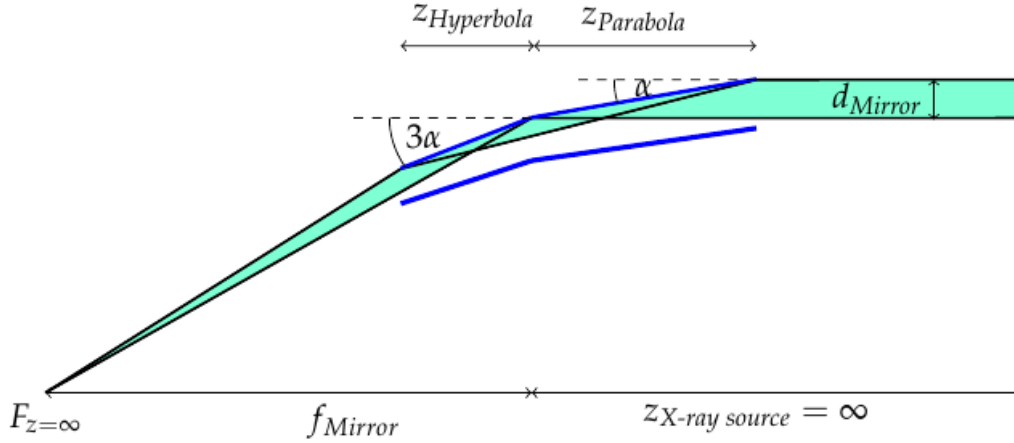


Figure 8: Ideal illumination of a Wolter type 1 telescope optic. The length of the hyperbola $z_{Hyperbola}$, the length of the parabola $z_{Parabola}$, and the distance d_{Mirror} between the mirror shells are optimized for X-rays which are parallel to the optical axis z . The distance to the X-ray source $z_{X-ray source}$ is ∞ .

The mirror modules are designed and manufactured in a way that the shells are packed as densely as possible. I.e. the distance between the mirror shells d_{Mirror} , the length of the parabola $z_{Parabola}$, and the length of the hyperbola $z_{Hyperbola}$ are optimized in such a way that the collecting area is maximized.

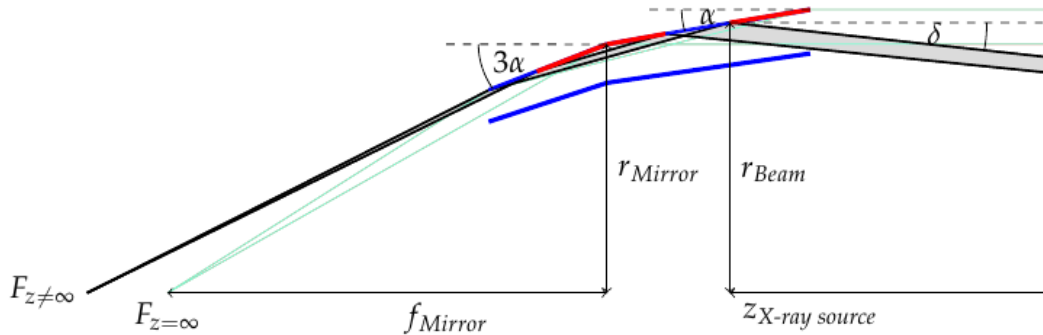


Figure 9: Divergent illumination of a Wolter type 1 telescope optic with a finite source distance $z_{X-ray source}$. The divergence δ relative to the optical axis is calculated as follows: $\delta = \text{atan}(r_{Beam}/z_{X-ray source})$. The distance to the optical axis is given by r_{Beam} . Compared to the ideal illumination, shown in Fig. 8 and indicated here in light blue, different areas of the parabola and hyperbola correspond. Additional, parts of the mirror cannot contribute to the focused point image. Non-sensitive areas are marked in red.

In the case of SPO the distance $d_{Mirror} = 775 \mu\text{m}$ is fixed and given by the wafer thickness. In order to maximize the collecting area of the SPO the axial length of each reflecting surface is calculated as follows: $z_{Parabola} = d_{Mirror} / \cos(\alpha)$. The condition for the length of the hyperbola results from the fact that all the light reflected from the parabola, is collected and can be reflected a second time. As a consequence of this design the SPO length decreases towards the outer edge of the telescope aperture, as shown in Fig. 4b.

Now the case is considered in which the SPO module is characterized using divergent light, schematically shown in Fig. 9. The divergence angle δ relative to the optical axis for a source with finite distance $z_{X-ray source}$ is calculated as follows: $\delta = \text{atan}(r_{Beam}/z_{X-ray source})$. In the case of a finite source distance the angle between the parabola and

incident light is then $\alpha' = \alpha + \delta$. Consequently, light is reflected at an angle of $2\alpha'$. Due to this larger angle two effects occur.

Firstly, an X-ray reflected by the parabola at an angle of $2\alpha'$ is reflected onto a different region of the hyperbola compared to the parallel illumination. The second reflection on the hyperbola is located closer to the edge of the mirror exit and the image is formed at a greater distance.

Secondly, parts of the mirror can not contribute to the focused point image. In the case of the SPO, light from the entrance of the parabola is not reflected by the hyperbola, as the hyperbolic mirror is too short for illumination with divergent light. In addition, inner shells shadow the region between the parabola and the hyperbola. To illustrate these effect the non-sensitive areas are marked in red in in Fig. 9.

With the current design [38] 42 % of the ATHENA optics can be illuminated at the PANTER X-ray test facility. The illumination can be optimized, by increasing the beam line length or by using a collimator. Calculated values are shown in Fig. 10. The present PANTER configuration is indicated by the red line.

Another way to optimize the illumination arises when segments of the telescope are measured. Each individual mirror segment can be aligned normal to the beam. Then the absolute divergence angle δ is reduced. However, this measurement method can only be used to determine the efficiency of the mirror. This measuring method is not suitable to determine the PSF, as the rotation causes off axis aberrations, which influence the PSF.

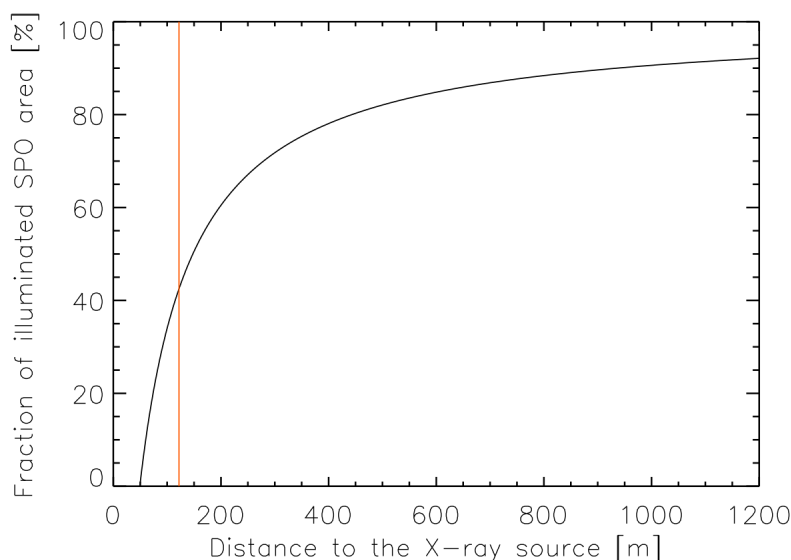


Figure 10: Illumination of ATHENA type optics. Due to a finite source distance the SPO can not be fully illuminated. With increasing the beam path length the full illumination can be approximated. With an object distance of 122 m as available at the PANTER X-ray test facility, indicated by the red line, 42 % of the ATHENA optics can be illuminated.

4.2. An X-ray collimator for ATHENA

The discussion of the previous section shows that with a collimator the measurement set-up at the PANTER X-ray test facility can be significantly improved. Specifically, the collimator should be used to characterize optics, such as those planned for ATHENA. The concept of the ATHENA optics, detailed discussed in Sect. 3.2, defines therefore the requirements the collimator has to meet.

As already mentioned in Sect. 3.2.2 the cross-section area of the collimated beam is determined by the aperture of a SPO module. Hence, a collimator aperture of $3\text{ cm} \times 10\text{ cm}$ is required. The angular resolution requirement for ATHENA is 5 arc sec. Aberrations due to the collimator must be negligible, in order to accurately determine the PSF of a mirror module. This requires that the resolution of the collimator is significantly better than that of the resolution of ATHENA. We postulate here that the resolution of the collimator should be at least one order of magnitude better than the resolution required for ATHENA. Consequently, we require a resolution of <0.1 arc sec for the collimator.

Requiring, that the resolution of the collimator is 0.1 arc sec, the *absorbing collimator* shown in Fig. 6a can be investigated. The divergence $\tan(\delta) = d_{\text{pinhole}}/l_{\text{Absorber}}$ can be calculated for a pinhole with diameter d_{pinhole} and the length of the absorbing part l_{Absorber} . As an example, this means that an absorbing part with a length of 1 m has holes with a maximum diameter of 500 nm. To fabricate such an *absorbing collimator* does not seem feasible or at least should be extremely challenging.

Alternatively, the collimator can, as in the optical wavelength regime, be realized with a lens, as shown in Fig. 6b. The physical concepts to realize X-ray lenses have been discussed in more detail in Sect. 3.1. The suitability of these physical concepts for an X-ray collimator will be examined in the following.

In the past, different X-ray collimator set-ups have been discussed. One was to use a flight spare mirror from the SOHO, that has a resolution of ≤ 1 arc sec [10]. It was proposed to place an X-ray source at the mirror focus. By employing the mirror module, used in the reverse direction, the X-ray beam is then collimated.

A second approach is a system of a parabolic mirror that uses grazing incidence to collimate the beam. A beam expander shall be used to increase the beam in size [32].

Both concepts are theoretically possible. However, a concept based on a grazing incidence mirror causes two major problems. One is, that in order to fulfill the requirement of a large area collimated beam either a beam expander or a nested mirror system has to be used. Another problem is caused by the requirement of a good angular resolution. Compared to existing X-ray optics (see Sect. 3.2.2) at least a resolution as good as that achieved for CHANDRA is needed for the collimator. Achieving such a resolution is possible, however at a non-negligible financial expense.

As an alternative to reflective optics in grazing incidence, there are two other physical principles that have not yet been taken into consideration in order to realize an X-ray collimator. As discussed in Sect. 3.1 X-ray optics can also be realized by making use of refraction or diffraction. Refractive optics, however, are generally unsuitable due to their concave shape.

As collimator optics a diffractive optical system like a ZP seems promising. Chromatic aberrations, a significant disadvantage for astronomy (see Sect. 3.2.1), are irrelevant in the collimator set-up, if not positive. Generally, the telescope optics are characterized using monochromatic X-rays. Consequently, it is sufficient if the source is monochromatic.

An advantage to use the ZP as a collimator is that the experimentally achieved angular resolutions are orders of magnitudes better than the angular resolutions of reflective X-ray optics. E.g. a multilevel silicon ZP, designed for a focal length of 110 m at the energy of the Cu-K $_{\alpha}$ line (8.04 keV), yielded an angular resolution of 20.5 milli arc sec. This ZP, with an aperture diameter of 3 mm, was measured at the GSFC [19].

Another advantage to using a ZP as collimator is that such optics in general can be used in transmission. Grazing incidence optics (e.g. Wolter optics) have in general larger off-axis aberrations [4] than a normal incidence optic (e.g. ZP). A detailed description, including off axis aberrations, of a ZP is given in Sect. 5.3. Due to the better off axis performance of a ZP, alignment requirements for the collimator set-up are weaker than for a X-ray collimator based on a grazing incidence optic.

In principle, a ZP seems to be an ideal collimator optic. Particularly unique is the required area the ZP. With a required collimated beam area of 3 cm \times 10 cm the ZP radius needs to be in the range of several centimeters. Comparable ZP, optimized for the energy range from 0.1 keV to 10 keV, have much smaller radii of 30 μ m [7] or 3 mm [19]. The development of such a large area ZP is an essential part of this report. In the next section we examine how a ZP theoretically suits as a collimator optic.

5. Zone Plate Optics

A zone plate (ZP) [9] is basically a circular diffraction grating with a radially increasing line density. Usually ZP are used in X-ray microscopy as imaging optics. In this report we investigate the suitability of using a ZP to collimate a divergent X-ray beam.

Schematically, the basic set-up is shown in Fig. 11. The ZP, with a focal length f_{ZP} , is placed at a distance f_{ZP} to the X-ray source. Since object distance g is equal to the focal length f the image distance b , calculated using the thin lens equation (2), is infinity and hence the diffracted beam is collimated.

Theoretically, there is no difference for what application a ZP is designed. However, using a ZP as a collimator some special requirements have to be taken into account. These requirements are theoretically elaborated in this section. Additional are calculated specific values for the ZP, which have been realized to build the ZPC. As the ZP design is strongly dependent on energy, the optical parameters discussed in the following are applied for the

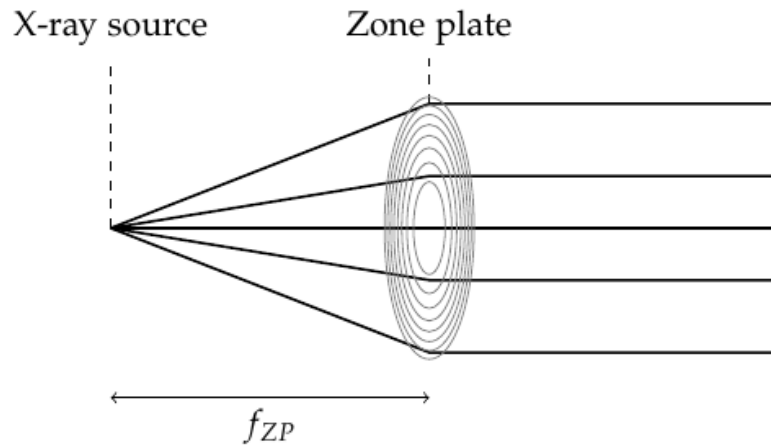


Figure 11: The ZPC set-up. The ZP is placed in a distance f_{ZP} to the X-ray source. According to Eq. (2) the image distance b is infinity and the diffracted beam is parallel.

Al- K_{α} emission line at $E = 1.49$ keV ($\lambda = 0.83$ nm), which is typically used to characterize Wolter optics. A detailed discussion of the X-ray energy selection is given in section 6.

The theory of ZP is described in detail in literature [1, 21] and the theoretic basics of a ZP optic are summarized in Sect. 5.1. An important parameter for a diffractive optic, and thus also for a ZP, is the diffraction efficiency. In Sect. 5.2.1 will be shown, how the efficiency of a ZP depends on the material and the geometry of the diffractive structure. Based on these theoretical elaborations we presented in Sect. 5.2.2 calculated values for the realized ZP. Additionally, the aberrations caused by deviations from the design in the manufacturing process and how these aberrations can be minimized are discussed.

A key parameter for an imaging optical system is its angular resolution. The resolution of a ZP is theoretically limited by diffraction. Experimentally, the resolution is, however, often limited by aberrations. Aberrations are caused mainly by alignment and manufacturing issues. The theoretical basics to quantify these aberrations is the OPD, which is discussed in detailed in Sect. 5.3.1. In Sect. 5.3.2 we discuss the experimental limits, calculated specifically for the ZPC set-up.

A special feature of a ZP is that it has multiple foci due to higher diffraction orders. These higher diffraction orders can enhance the background in the collimator configuration. However, using geometrical considerations (Sect. 5.4) there are two possible solutions to reduce such a background contribution.

5.1. Basic formulas for the ideal zone plate ZP

The structure of a ZP has to fulfill the condition, that light emitted at the point Q is focused at the point P . This means for a diffractive optic, that at P all rays with wavelength λ have to interfere constructively. Fig. 12 shows a schematic of how to calculate the optical path difference (OPD). In order to get constructive interference from the

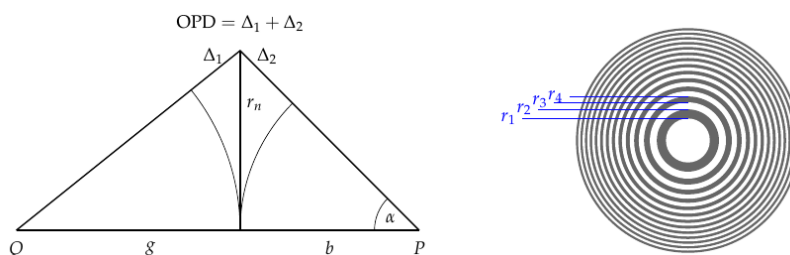


Figure 12: Sketch to calculate the (). (Left) The schematic light path. Light, emitted at point Q , is focused at the image point P . Notations used by the basic ZP equations are illustrated. (Right) Schematic of a ZP.

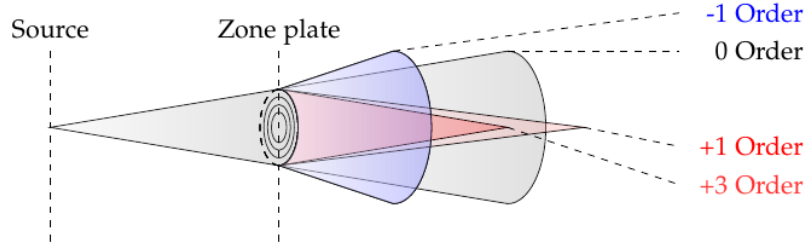


Figure 13: Schematic of ZP diffraction patterns. Higher order foci exist and are located along the optical axis.

OPD, which oscillates between 0 and 2π , a fraction has to be blocked, e.g. phases between 0 and π . This yields for a ZP in a periodic structure of opaque (or phase shifting) and transparent zones. The boundary radius r_n of the n^{th} zone (with $n \in \mathbb{N}$ and r_n is alternating the inner radius of opaque and transparent zones) is then calculated using the OPD between a ray passing on the optical axis and a ray passing the ZP at r_n . Using the notation of Fig. 12 and the condition of constructive interference in P that the $\text{OPD} = n\lambda/2$ the radii r_n of a ZP are calculated using the following Eq. (3).

$$\text{OPD} = \Delta_1 + \Delta_2 = \sqrt{g^2 + r_n^2} - g + \sqrt{b^2 + r_n^2} - b = n\lambda/2 \quad (3)$$

After appropriate transformation of Eq. (3) the radius of the n^{th} Fresnel zone is calculated as:

$$r_n^2 = \frac{[4gb(g+b)]n\lambda + [gb + (g+b)^2]n^2\lambda^2 + [(g+b)/2]n^3\lambda^3 + [1/16]n^4\lambda^4}{4(g+b)(n\lambda + (g+b)) + n^2\lambda^2} \quad (4)$$

For the case of a soft X-ray ZP $\lambda \approx 1 \times 10^{-9}$ m is small compared to $g \geq 1$ m and $b \geq 1$ m and also $n\lambda \ll g+b$. With these assumptions Eq. (4) simplifies and can be expressed with the focal length f by using the thin lens equation:

$$\frac{1}{f} = \frac{1}{g} + \frac{1}{b} \Leftrightarrow f = \frac{gb}{g+b} \quad (5)$$

to:

$$r_n^2 = \frac{gbn\lambda}{g+b} = n f \lambda \quad (6)$$

As a ZP is a diffractive optic, higher order diffraction patterns are formed. Substituting in the optical path length calculation n with $n \cdot m$, with $m \in \mathbb{Z}$, the order dependent focal length f_m , with $f_m = f/m$, can be introduced. Fig. 13 illustrates how the higher order foci are located along the optical axis. Besides the first order focus an infinite number of real (m positive) and virtual (m negative) foci exist. The not diffracted direct beam corresponds to $m = 0$.

For the so far discussed ZP configuration it can be shown that higher order foci exist for odd m , while even orders (m even) they are canceled out. However, even order foci can occur by changing the design of the ZP. A more detailed discussion in Sect. 5.2 includes the intensity dependent contribution of the diffraction orders.

Some useful quantities follow from the fundamental ZP Eq. (6). By differentiating Eq. (6) the width dr_n of zone n can be calculated by setting $dn = 1$ so that $2r_n dr_n = \lambda f$. Defining the first zone boundary $r_1 \equiv \sqrt{\lambda f}$ the width of the n^{th} zone can be expressed as follows:

$$dr_n = \frac{r_n}{2n} = \frac{r_1}{2\sqrt{n}} \quad (7)$$

Assuming that the number of zones is sufficiently large, i.e. $N > 100$ [21], the diffraction pattern at the focus approximates an Airy pattern, and hence the resolution of the ZP is diffraction limited. The resolution δ_m at the focus f_m is then given by the Rayleigh criterion:

$$\delta_m = \frac{0.61\lambda}{\text{NA}} = 1.22 dr_N / m \quad (8)$$

$$\text{NA} \equiv n \sin(\alpha) \approx 1 \cdot \tan \alpha = \frac{r_N}{f_m} = \frac{\lambda m}{2 dr_N} \quad (9)$$

The numerical aperture NA is defined with the index of refraction n , which is for soft X-rays set to 1. The aperture angle α is defined in Fig. 12. Eq. (8) shows, that the resolution depends on the width of the outermost zone dr_N and can be improved for higher orders. The theoretical resolution can be improved [30] by using a central obstruction. This, however, is more of theoretical interest, as aberrations, which are discussed in Sect. 5.3, dominate the resolution of the ZPC.

5.2. Diffraction Efficiencies

The diffraction efficiency measures how much optical power is diffracted into a designated direction compared to the power incident onto the ZP. The efficiency of a ZP is dependent on the material and the geometry of the structure. To simplify the geometry a rectangular profile, as shown in Fig. 14, is assumed in the following. Based on the mathematical description of such a profile, the theoretical limits of the diffraction efficiency are determined in Sect. 5.2.1.

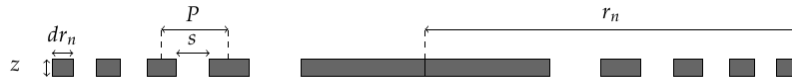


Figure 14: Schematic of a ZP with rectangular profile. The symbols are defined in Table 1.

In addition to the theoretical diffraction efficiencies, we determine specific values for the ZPC configurations in Sect. 5.2.2 and show how a variation of the material affects the parameters for the fabrication and efficiency. Based on these results, we identify suitable materials for the ZPC. For two suitable materials variations in the geometry and their influence on the efficiency are discussed. Based on these results, we determine fabrication tolerances for these two materials.

5.2.1. The diffraction efficiency - theoretical limits

The efficiencies for a ZP with a rectangular profile, shown schematically in Fig. 14, are calculated for orders $m \neq 0$ according to [16, 28]:

$$\frac{I_{m \neq 0}}{I^0} = \left(\frac{\sin(m\pi \frac{s}{P})}{\pi m} \right)^2 \cdot [1 + e^{-2k\beta z} - 2e^{-k\beta z} \cos(k\delta z)] \quad (10)$$

The first term describes the diffraction pattern of a slit with width s . The second term takes into account the phase shift and the absorption by the material. The following applies to the zeroth diffraction order $m = 0$:

$$\frac{I_{m=0}}{I^0} = \left(\frac{s}{P} \right)^2 + \left(1 - \frac{s}{P} \right)^2 e^{-2k\beta z} + 2 \left(\frac{s}{P} \right) \left(1 - \frac{s}{P} \right) e^{-k\beta z} \cos(k\delta z) \quad (11)$$

The necessary parameters, to calculate the diffraction efficiencies, used in Eq. (10) and Eq. (11), are summarized in Table 1. Eq. (10) enables to calculate the diffraction efficiencies of a ZP with rectangular profile for an arbitrary material. Two configurations are presented in the following, which are discussed in more detail in literature. The two special cases are known as the Fresnel ZP and the Rayleigh-Wood ZP in literature. The parameters and diffraction efficiencies of both are given in Table 2.

Common to both is a maximum first order intensity $I_{m=\pm 1}$ by using a space to period ratio of $s : P = 0.5$. They differ considerably in the refractive index $n = 1 - \delta - i\beta$ of the material, which have been introduced in section 3. The Fresnel ZP, shown schematically in Fig. 15a, assumes opaque marks. That means that the marks are completely absorbing ($e^{-k\beta z} = 0$). The first order efficiency is calculated to $I_{\pm 1}/I^0 = 1/(\pi)^2 \approx 10\%$.

The phase reversal Rayleigh-Wood ZP [25, 43, 16], shown schematically in Fig 15b, assumes a non absorbing material ($\beta = 0$), and a profile height $z = 0.5\lambda/\delta$. Hence, the marks give a π phase-shift while having zero absorption. The result is that the intensities of odd diffraction orders are increased by a factor of four at the expense of the zero order intensity. The first order intensity is calculated to $I_{\pm 1}/I^0 = 4/(\pi)^2 \approx 41\%$. This efficiency value gives also the theoretical limit for a ZP with rectangular profile.

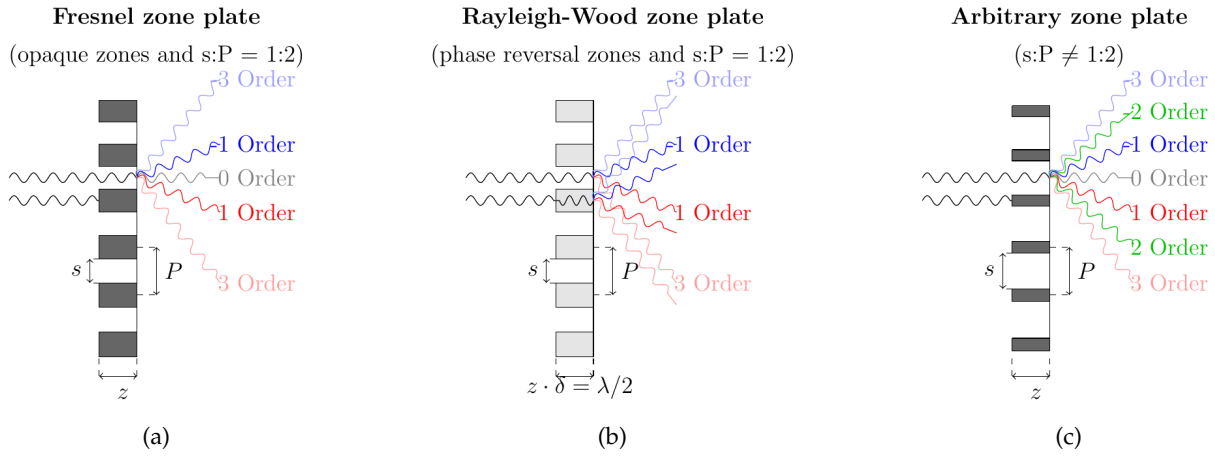


Figure 15: Schematic of different ZP types: (a) The Fresnel ZP, having opaque marks, provides a first order efficiency of $\approx 10\%$. (b) The Rayleigh-Wood ZP, having phase shifting marks, provides a first order efficiency of $\approx 41\%$. (c) The arbitrary ZP has a space to period ratio $s : P \neq 1 : 2$. Hence, even diffraction orders occur.

It has to be considered that in the soft X-ray regime it is not possible to find materials, which have no absorption. Hence, a compromise between phase-shift and absorption must be made. Summarizing the discussion of material, theoretically the Fresnel ZP gives the lower efficiency limit of 10% and the Rayleigh-Wood ZP the upper limit of 41%.

In addition to the material, the geometry of the ZP affects the efficiency. This discussion is important, as especially the fabrication can influence the geometry leading to thickness z and the space to period ratio $s : P$ variations. Since z occurs in Eq. (10) as a factor of the refractive index, it can be considered analogous to a change in the refractive index. The ratio $s : P$ affects only the front part of Eq. (10). Any deviation from the value of $s : P \neq 0.5$ leads to a reduced first order intensity. Roughly speaking, the first order intensity loses efficiency at the expense of even diffraction orders. This is schematically shown in Fig. 15c by the appearance of diffraction order $m = 2$. For the sake of completeness it should be mentioned that the intensity of $I_{m=+1}$ can be increased by using a blazed profile. With a triangular profile, instead of the rectangular profile as used for the Fresnel and Rayleigh-Wood ZP, the intensity of $I_{m=+1}$ is increased at the expense of $I_{m=-1}$.

5.2.2. The diffraction efficiency - calculations for the ZPC

Here we calculate specific diffraction efficiencies based on the theoretical considerations presented in the previous section. The influence of the material through its refractive index on the diffraction efficiency is examined. By maximizing the first order diffraction efficiency an optimal profile height z_{opt} , depending on material, can be obtained. Additionally, the parameters z and $s : P$ are examined in order to study the influence of manufacturing processes.

Table 1: Definition of characteristic ZP parameters to calculate the diffraction efficiencies.

Symbol	Description
$s = r_n - r_{n-1}$	space
$P = r_n - r_{n-2}$	period
z	profile height
$n = 1 - \delta - i\beta$	index of refraction
δ	index decrement
β	absorption coefficient
$k = 2\pi/\lambda$	wave number
λ	wavelength

Table 2: Parameters for ideal ZP configurations and the corresponding theoretic diffraction efficiencies.

	Fresnel	Rayleigh Wood
s:P	1 : 2	1 : 2
$k\beta z$	$\gg 1$	0
$k\delta z$	arbitrary	π
$I_{m=0}/I^0$	25 %	0 %
$I_{m=\pm 1}/I^0$	$\approx 10\%$	$\approx 40\%$
$I_{m=odd}/I^0$	$1/(m\pi)^2$	$4/(m\pi)^2$
$I_{m=even}/I^0$	0 %	0 %

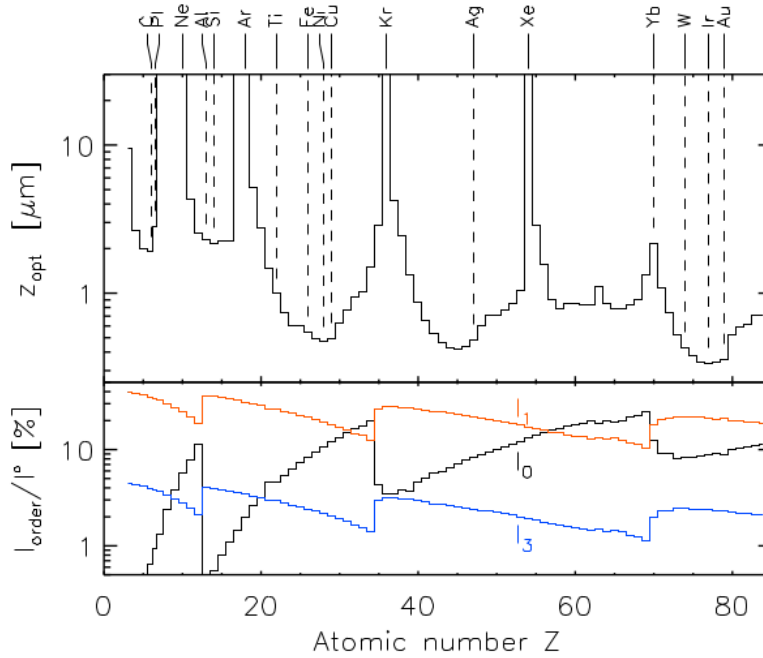


Figure 16: Element properties for a ZP optimized for the the Al- K_{α} emission line at 1.49 keV. Top: The thickness z_{opt} to get a maximal first order intensity derived by the derivation of Eq. (10) $\partial I_{m=1}/\partial z = 0$. Bottom: The corresponding order intensity relative to the incoming beam intensity. The values here are calculated for standard conditions of temperature and pressure. That is, for a temperature of 273.15 K (0.00 °C) and a pressure of 100 kPa (0.987 atm). The values are based on the tabulated values for δ and β [12].

In the particular case of a collimator the ZP has to be optimized for one wavelength. Therefore, a monochromatic source is assumed in the following. The basis for the calculations is the Al- K_{α} emission line at $E=1.49$ keV ($\lambda = 0.834$ nm).

The optimal profile height z_{opt} , with respect to the efficiency, can be determined by differentiating Eq. (10) $\partial I_{m=1}/\partial z = 0$. The profile height for elements with atomic number Z from 6 to 83 is shown in the top panel of Fig. 16. Except for (noble) gases z_{opt} is in the range of 0.1 μm to 10 μm and in general with increasing Z the profile height decreases. The thickness z_{opt} , depending on the material, influences also the fabrication. The ratio between the zone width dr_n and profile height z_{opt} is called the aspect ratio. The aspect ratio is an important measure since the possibility to fabricate high aspect ratios is one major limitation.

The first order intensity, shown in the bottom panel of Fig. 16, is in the range of 10 % to 40 %, as expected from the theoretic description of a ZP with rectangular profile presented in Sect. 5.2.1. The highest intensity is achieved for low Z materials and the first order intensity in general decreases with increasing Z . However, some materials are more suitable in sense of first order efficiency than others. The steps in the first order intensity are due to photoelectric

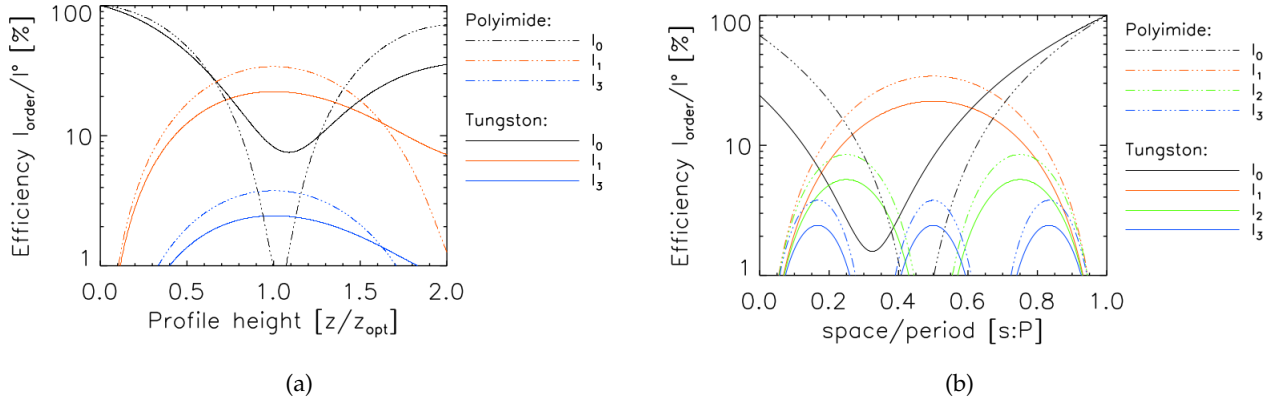


Figure 17: The dependency of the efficiency on the geometry: (a) on the profile height z (b) on the space to period ratio $s : P$.

absorption by K, L, or M shell electrons. Hence, for some materials the absorption coefficient β dominates the phase shifting index decrement δ .

For the fabrication of the ZPC two materials with $\delta \gg \beta$ are investigated and first order diffraction efficiencies are calculated for the Al- K_{α} emission line. One material is PI, a chemical compound consisting of elements with low Z with structural formula C₂₂H₁₀N₂O₅. PI achieves a maximum theoretical efficiency of 34 %, with a profile height of 2.8 μm . The second material is tungsten (W) which achieves a lower theoretical efficiency of 22 %, at a lower profile height of 0.422 μm . This lower profile height results in lower aspect ratios, an advantage in manufacturing.

Geometric parameters that affect the diffraction efficiency, are the profile height z and the ratio $s : P$ ⁴. Below it will be examined how an error in the profile height Δz or an error in the ratio $\Delta s : P$ affects the efficiency of the collimator. Moreover, tolerances for fabrication for Δz and $\Delta s : P$ are determined.

Deviations of the geometry can occur both globally and locally. The global values for z and $s : P$ are usually chosen so that the efficiency is maximized. Consequently, a global error in one of the variables leads to a reduced efficiency of the collimator. A local error leads to inhomogeneities in the collimated beam. Local changes in intensity are described by the derivation of Eq. (10). The local changes in the intensity are zero when the intensity is maximum. Consequently, the manufacturing tolerances Δz and $\Delta s : P$ are lax for $s : P = 0.5$ and for $z = z_{\text{opt}}$.

The theoretical mathematical description of the geometry, and thus the tolerances of fabrication, will now be shown for actual values. For this, the dependencies of the efficiency on the profile height $I(z)$ and the $s : P$ ratio $I(s : P)$ are investigated.

The dependence of the efficiency on the profile height $I(z)$ is shown for PI and W in Fig. 17a. Eq. (10) implies that $I(z) \propto e^{-2k\beta z} - 2e^{-k\beta z} \cos(k\delta z)$. $I(z)$ is a damped oscillation with maximum at $z = z_{\text{opt}}$. The damping is given by the absorption coefficient β . For $\lim_{z \rightarrow \infty} I(z) = 10\%$ results in the efficiency of the Fresnel ZP. The deviation of the efficiency is obtained from the derivative of Eq. (10). Since it can be assumed that $\delta \gg \beta$ (for both materials at 1.49 keV) the derivative can be simplified to: $\partial I_{m=1}/\partial z \propto \sin(k\delta z)$. A minimal deviation of the efficiency, and therefore a maximum tolerance of the profile height Δz , derives for a profile height $z = z_{\text{opt}}$.

The dependence of the efficiency on the $s : P$ ratio $I(s : P)$ is shown for PI and W in Fig. 17b. Eq. (10) implies that $I(s : P) \propto (\sin(\pi \frac{s}{P}))^2$ with a maximum at $s : P = \frac{1}{2}$. For the derivation it follows that $\partial I_{m=1}/\partial s : P \propto \sin(\pi \frac{s}{P}) \cos(\pi \frac{s}{P})$. A minimal deviation of the efficiency, and therefore a maximum tolerance of the ratio $s : P$, derives for a ratio of $s : P = 0.5$.

As a side note to the ratio $s : P$ it should be mentioned that for some applications a ratio $s : P < 0.5$ is appropriate. Such an application is for example, if the contribution of diffraction order $m = 0$ is regarded as a background. From Eq. (11) it follows that $I_{m=0}$ has a material-dependent minimum at $s : P < 0.5$. This can be clearly seen in Fig. 17b. Consequently, the background can be reduced by a suitable choice of $s : P$. For the ZPC the problem of the background is solved purely geometrical, detailed discussed in Sect. 5.4. Therefore, a ratio of $s : P = 0.5$ is in general used for the fabrication.

⁴ Pure period error does not affect the efficiency. Period errors leads to aberrations in the angular resolution, which are discussed in Sect. 5.3

Table 3: Manufacturing tolerances for a ZP. For requirements on the homogeneity of the beam I_{hom} fabrication tolerances for Δz and $\Delta s : P$ are determined. It is assumed a ZP with maximum efficiency for the first diffraction order I_{max} will be manufactured. Independent of the material the space to period ratio is $s : P = 0.5$ and the profile height is z_{opt} . For the PI ZP that results in a profile height of $z = 2830$ nm and $I_{max} = 34\%$. For the W ZP that results in a profile height of $z = 427$ nm and $I_{max} = 22\%$.

	$s : P$	PI		W	
		Δz	$\Delta z / z_{opt}$	Δz	$\Delta z / z_{opt}$
$I_{hom} > 0.99 \cdot I_{max}$	0.5 ± 0.031	185 nm	6.5 %	25.8 nm	7.5 %
$I_{hom} > 0.95 \cdot I_{max}$	0.5 ± 0.071	415 nm	14.7 %	57.9 nm	16.8 %
$I_{hom} > 0.90 \cdot I_{max}$	0.5 ± 0.102	591 nm	20.8 %	81.2 nm	23.6 %

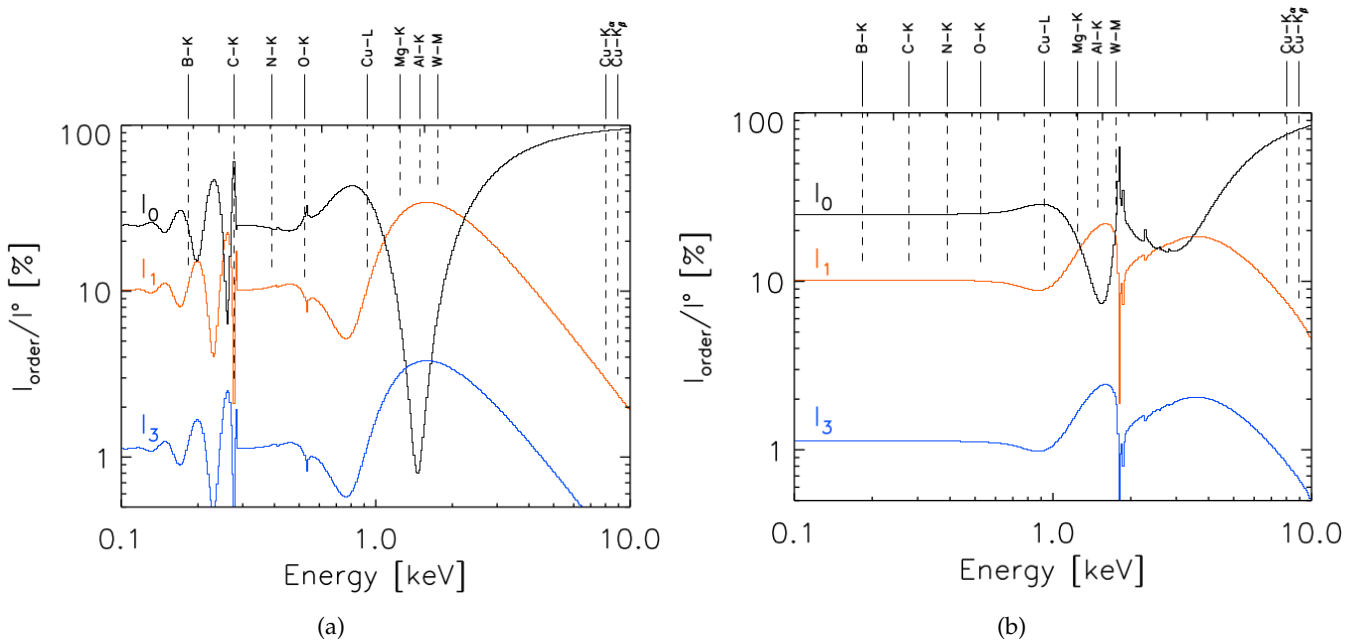


Figure 18: The energy dependence of a phase ZP with optimal thickness $d = d_{\lambda/2}$ for PI (a) and W (b). The ZP is optimized for an energy of 1.49 keV, the Al- K_{α} emission line. In general for low energy photons the ZP marks are absorbing and the ZP show the performance of a Fresnel ZP, while for high energy photons the ZP becomes transparent and the diffraction efficiencies for orders $m \neq 0$ decrease.

Values for tolerances in fabrication can now be given based on the previous considerations. Global errors lead to a reduced efficiency, which can easily be compensated by a higher intensity of the source or longer integration time. Local errors, which lead to inhomogeneities in the beam, can be retrospectively compensated only with great effort. Therefore, these errors must be taken into account when manufacturing. To calculate the tolerances Δz and $\Delta s : P$ a limit to the efficiency of I_{hom} is defined. Tolerances for different limits of homogeneity I_{hom} are calculated in Table 3. They are based on the assumption that $z = z_{opt}$ and $s : P = 0.5$. Hence, $I = I_{max}$ and the global errors are assumed to be zero. Consequently, the tolerances for Δz and $\Delta s : P$ will be lower if a global error occurs.

So far the ZP diffracting have been discussed for one energy, the Al- K_{α} emission line $\lambda = 0.83$ nm ($E = 1.49$ keV). Considering, that the PANTER X-ray test facility provides a set of X-ray sources in the range of 0.1 keV to 10 keV, it might be interesting to get a closer look at the energy dependence of the thus optimized ZP. Fig. 18 summarizes the diffraction efficiencies depending on energy for ZP with PI and tungsten phase shifting structures. In general, for low energy photons the ZP marks are absorbing and the ZP shows the performance of a Fresnel ZP, while for high energy photons the ZP becomes transparent and the diffraction efficiency is low.

5.3. Angular resolution

In general, the term resolution refers to the distinctness of fine structures, e.g. the smallest still observable distance between two point-like objects. By specifying an angular resolution, it can be quantified. In the case of the ZPC the resolution describes the parallelism of the beam. Theoretically, the resolution, and thus, the parallelism of the beam is diffraction limited.

In reality, the resolution is limited by aberrations. These aberrations can be studied using geometric optics. In the case of a ZP, the optical path difference (OPD) is typically used to calculate the aberrations. In order to determine aberrations, the calculation of the OPD, introduced in Sect. 5.1, is generalized in Sect. 5.3.1.

Using the more generalized form of the OPD we identify possible aberrations. These are for the ZPC the alignment, the fabrication, and properties of the X-ray source. The resulting angular errors, and thus deviations from a parallel beam, are calculated in Sect. 5.3.2

5.3.1. Theoretical basis - the general OPD

Aberrations can be determined with the OPD. In order to account for aberrations, such as the alignment, the calculation of Sect. 5.1 is generalized. This means, in particular, that the chief ray is not necessarily normal to the ZP and that the distance between the source and the ZP is not necessarily equal the ZP focal length f .

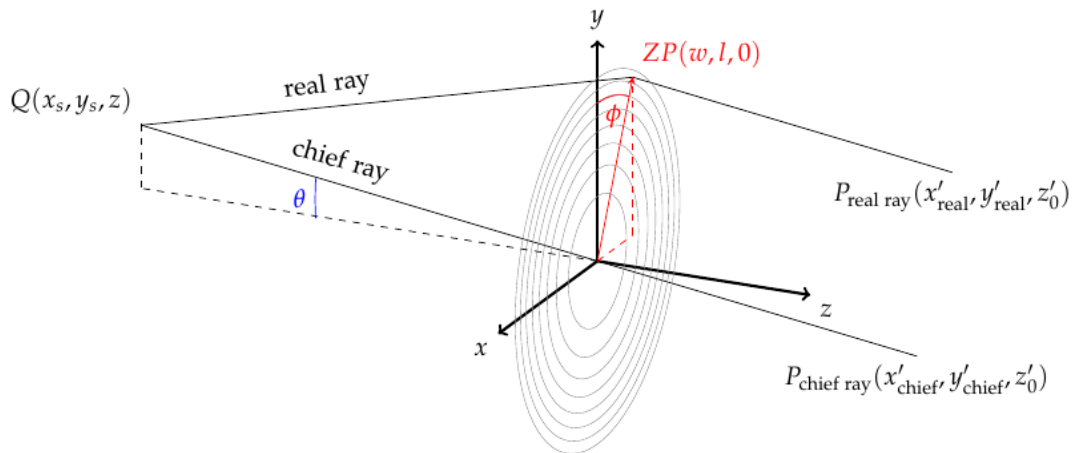


Figure 19: Schematic to calculate the OPD of a ZP including off axis aberrations. This means, in particular, that the chief ray is not necessarily normal to the ZP and that the distance between source and ZP is not necessarily equal the ZP focal length f . The source at Q is off axis at an angle θ to the ZP normal. The point $P(x', y', z')$ can be identified as the Gaussian image point. A real ray is diffracted by the ZP at the point $ZP(w, l, 0)$.

A schematic drawing illustrates this set-up in Fig. 19. A Cartesian coordinate system with the ZP center defining the origin is used. The ZP is located in the $x - y$ plane and the optical axis is the z axis. The source at $Q(x = x_s, y = y_s, z_s)$ is off axis at an angle θ to the ZP normal. The point $P(x = x', y = y', z = z')$ will later be identified as the Gaussian image point. A real ray is diffracted by the ZP at the point $ZP(x = w, y = l, z = 0)$. The OPD is calculated analogous to Howells [13]. Terms up to the fourth order are taken into account. The OPD is then given by the following term:

$$\begin{aligned}
 \text{OPD} = & \underbrace{\frac{w^2 + l^2}{2} \left[\frac{1}{z} + \frac{1}{z'} \right]}_{2^{\text{nd}} \text{ order term}} - \underbrace{\frac{(w^2 + l^2)^2}{8} \left[\frac{1}{z^3} + \frac{1}{z'^3} \right]}_{4^{\text{th}} \text{ order terms}} \\
 & + \underbrace{\left(-\frac{l^2}{2} + \frac{w^2 + l^2}{4} \right) \theta^2 \left[\frac{1}{z} + \frac{1}{z'} \right] + \frac{(w^2 + l^2)l}{2} \theta \left[\frac{1}{z^2} + \frac{1}{z'^2} \right]}_{4^{\text{th}} \text{ order terms}}
 \end{aligned} \quad (12)$$

In contrast to Sect. 5.1 fourth order terms are considered for the generalized form. For clear presentation Eq. (12) is simplified. The special case, when P is the Gaussian image point, is presented. In the collimator the set-up this results in $z = f$ and $z' = \infty$. The ZP coordinates w and l are transformed to their polar representatives. Hence, Eq. (12) becomes:

$$\begin{aligned}
 \text{OPD} = & \underbrace{\frac{1}{2} \frac{r^2}{f}}_{\text{defocus}} - \underbrace{\frac{1}{8} \frac{r^4}{f^3}}_{\text{spherical aberration}} + \underbrace{\left[-\frac{\sin^2 \phi}{2} + \frac{1}{4} \right] \frac{r^2}{f} \theta^2}_{\text{astigmatism and field curvature}} + \underbrace{\frac{\sin \phi}{2} \frac{r^3}{f^2} \theta}_{\text{coma}}
 \end{aligned} \quad (13)$$

The 2^{nd} order term is used to calculate the influence of a defocus. Assuming that the distance between the source at Q and the zone plate $ZP(w, l, 0)$ is not equal to f , a tolerance for the focal depth Δf can be introduced. The OPD, including a defocus term, results then in:

$$\text{OPD} = \frac{1}{2} \frac{r^2}{f + \Delta f} \quad (14)$$

Setting $\text{OPD} = n\lambda/2$ and $\Delta f = 0$ this expression can be identified as Eq. (6), the construction rule of ZP boundary radii.

The 4^{th} order terms represent Seidel type aberrations.⁵ These are separately investigated below.

The spherical aberration term expands Eq. (6) by considering fourth order terms. The OPD of the spherical aberration term is calculated to be:

$$\text{OPD} = \frac{1}{8} \frac{r^4}{f^3} \quad (15)$$

The spherical aberration term is especially important for large zone numbers n . A ZP can be corrected for spherical aberrations by modifying Eq. (6) by considering the fourth order terms of Eq. (13). Setting $\text{OPD} = n\lambda/2$ and taking account of spherical aberrations the n^{th} ZP radius r_n is then:

$$r_n^2 = n\lambda f + n^2 \lambda^2 / 4 \quad (16)$$

Terms depending on θ represent off axis aberrations. In the set-up discussed here, these terms are interpreted as an off axis alignment of the ZP with respect to the X-ray source. The astigmatism and field curvature term depends on θ^2 . The OPD is calculated to:

$$\text{OPD} = \left[\frac{\sin^2 \phi}{2} + \frac{1}{4} \right] \frac{r^2}{f} \theta^2 \quad (17)$$

The coma term depends on θ . The OPD is calculated to be:

$$\text{OPD} = \frac{\sin \phi}{2} \frac{r^3}{f^2} \theta \quad (18)$$

The aberrations considered thus far describe achromatic effects on the OPD. In addition, chromatic errors occur. The spectral bandwidth $\Delta\lambda$ is, in the case of the ZPC, given by the X-ray source⁶. Assuming a finite bandwidth $\Delta\lambda$, it can be shown, that the relative bandwidth of the source is simply equal to a relative change in focal length:

$$\frac{\Delta\lambda}{\lambda} = \frac{\Delta f}{f} \quad (19)$$

⁵ The distortion term vanishes in the OPD and hence a ZP is a distortion free optic.

⁶ In principle $\Delta\lambda$ can be limited by the detector. However, the relative bandwidth of the source is generally much better than that of the detector.

Consequently, chromatic errors correspond to an error of the focal length.

All previous aberrations assume a perfectly structured ZP. In Sect. 5.2 it was shown that a profile height error and a space to period error affect the efficiency. In addition, period errors can occur, which influence the resolution. For example, a distortion of the structure leads to a period error. Period errors lead to aberrations, since the period p depends on the radius of a ZP. From Eq. (6) follows:

$$p = \frac{\lambda f}{r} \quad (20)$$

Assuming, for example, a distortion by Δr , the OPD is calculated to be:

$$\text{OPD} = \frac{1}{2} \frac{(r + \Delta r)^2}{f} \quad (21)$$

With the calculations shown so far, the OPD can be computed for different types of aberrations. A quantitative description of the resulting angular aberrations follows in the next section.

5.3.2. Aberrations - the Quantitative Description

The general form of the OPD from Eq. (13) makes it possible to calculate the aberrations. Based on these calculations and with the given requirements for the angular resolution, the error of the aberrations can be estimated. The requirements for the collimator, and thus, the tolerances for the alignment and the fabrication, can be formulated in different ways.

Considering the collimator from a purely theoretical point of view, it is limited by the resolution of the ZP. Aberrations that affect the resolution can be neglected if their contribution to the OPD is smaller than $\lambda/4$. This concept, known as Rayleigh $\lambda/4$ concept, leads to requirements that are listed in the middle column of Table 4. The tolerances are determined in line with Young [44]:

$$\text{OPD} = \frac{n\lambda}{2} \pm \frac{\lambda}{4} \quad (22)$$

Considering the collimator to be used at PANTER, greater tolerances can be justified. We take as a requirement of the parallelism that the angular resolution of the ZPC is significantly (for example a factor of 10) better than the resolution of the telescope optics. This results generally in much larger tolerances, and thus, the larger tolerances for the alignment lead to a substantial simplification in the set-up.

To calculate these larger tolerances we use the concept of ray aberrations. Analogous to Howells [13] the optical path function $F = \text{OPD} - n\lambda/2$ is introduced. For a normal incidence optic the aberrations $\Delta x'$ and $\Delta y'$ are given by the following expression [2]:

$$\Delta x' = z'_0 \frac{\partial F}{\partial w}, \quad \Delta y' = z'_0 \frac{\partial F}{\partial l}$$

In angular resolution δ_x, δ_y these errors can be expressed as:

$$\delta_x = \frac{\partial F}{\partial w}, \quad \delta_y = \frac{\partial F}{\partial l} \quad (23)$$

Applying Eq. (23) to the aberrations identified in Sect. 5.3.1 individually, the contribution of the aberrations can be calculated. In Table 4 are summarized the corresponding errors to the image quality of the ZPC.

The image quality and possible aberrations, depending on the ZP radius, are shown in Fig. 20. The calculations can be applied to a ZP, designed with a focal length $f = 122$ m (i.e. the length of the PANTER X-ray beam line) at the Al- K_α emission line. Both design parameters are discussed in detail in section 6.

The red line indicates the diffraction limited resolution of the ZPC according to Eq. (8). The orange line indicates aberrations caused by the natural line width of the Al- K_α emission line ($\Delta E = 0.49$ eV) [18]. With these two solid lines, the lower resolution limit of the ZPC discussed here is given. Requiring a ZPC making a resolution of 0.1 arc sec, which is significantly better than the resolution of ATHENA type optics with 5 arc sec, makes ZP radii up to 0.2 m possible.

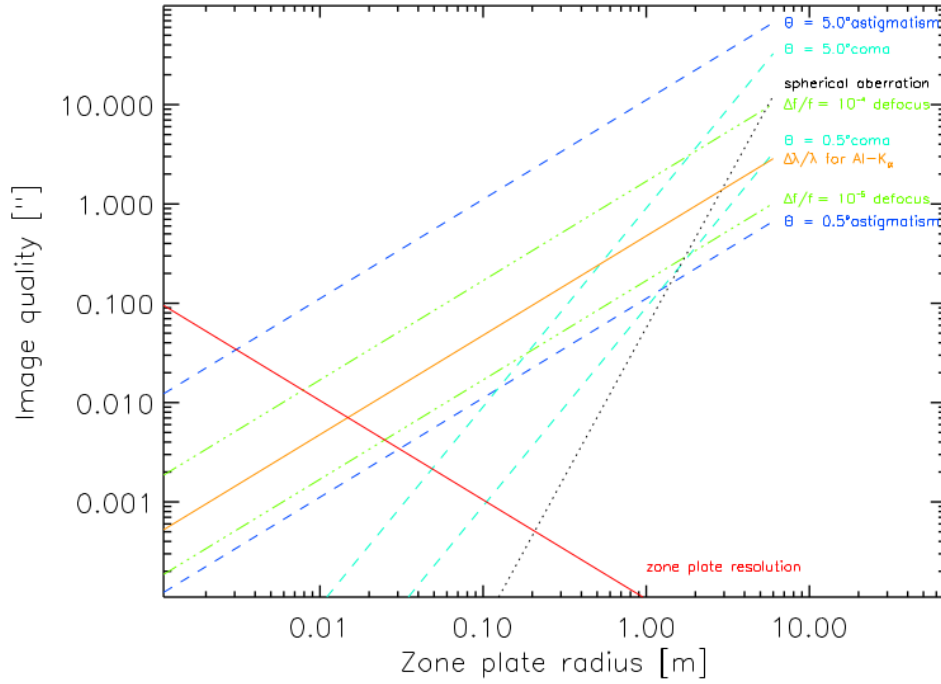


Figure 20: The angular resolution of a ZPC with $\lambda = 0.834$ nm and $f = 122$ m. The solid lines indicate the lower limit of the angular resolution. The red line indicates the diffraction limit. The orange line indicates chromatic aberrations caused by the natural line width of the Al- K_{α} emission line ($\Delta E = 0.49$ eV) [18]. The black dotted line indicates contributions caused by spherical aberrations. The remaining errors indicate alignment errors.

Table 4: Geometric aberrations of a ZP using paraxial approximation.

	Rayleigh $\lambda/4$ criteria	In angular resolution
focal depth	$\Delta f = \frac{1}{2} \frac{\lambda f^2}{r^2}$	$\delta = \frac{\Delta f}{f} \frac{r}{f}$
chromatic aberrations	$\Delta \lambda = \frac{1}{2} \frac{\lambda^2 f}{r^2}$	$\delta = \frac{\Delta \lambda}{\lambda} \frac{r}{f}$
radial error	$\Delta r = \frac{1}{4} \frac{\lambda f}{r}$	$\delta = \frac{\Delta r}{f}$
spherical aberrations	$n = \sqrt{\frac{2f}{\lambda}}$	$\delta = \frac{1}{2} \frac{r^3}{f^3}$
astigmatism & field curvature	$\Delta \theta = \sqrt{3n}$	$\delta = \frac{1}{2} \frac{r}{f} \theta^2 \sqrt{1 + 2 \sin^2(\phi)}$
coma	$\Delta \theta = \sqrt{\frac{f}{n\lambda}} \cdot \frac{1}{2n}$	$\delta = \frac{1}{4} \frac{r^2}{f^2} \theta \sqrt{1 + 8 \cos^2(\phi)}$

The black dotted line indicates contributions caused by spherical aberrations. Spherical aberrations can be avoided, by using Eq. (16) for the construction of ZP boundaries. However, this seems to be obsolete as the spherical aberration term becomes significant (>0.1 arc sec) for ZP radii >1 m.

The remaining errors indicate alignment errors. The dash dotted green lines indicate a defocus. The dashed blue lines indicate off axis aberrations. Requiring that the contribution of alignment errors is maximal 0.1 arc sec, specific values can be calculated. As alignment errors increase with radius, the following tolerances for alignment errors are applicable for the maximal reasonable ZPC radius of 0.2 m. The requirement of ≤ 0.1 arc sec leads to a precision of the focal positioning of $\Delta f = 36$ mm. The alignment tolerance for off axis errors is given by the astigmatism & field curvature term. It is calculated to $\theta = 1^\circ$. Both alignment tolerances can be met at the PANTER X-ray test facility.

Additional, there might be aberrations caused by the manufacturing process. Formally, these aberrations were taken into account with Eq. (21). However, these errors are not considered here in detail, as they are highly dependent on the manufacturing process. They must be considered separately during the fabrication process.

Summarizing, a ZPC at the PANTER X-ray test facility is feasible in sense of angular resolution. Requiring a resolution of 0.1 arc sec it has been shown that an outer ZPC radius of 20 cm is possible. With such a radius, one can illuminate a sufficient large area to cover an ATHENA type optic.

5.4. Avoiding background: geometric solutions

It has been discussed in Sect. 5.1 that a ZP has multiple foci. The contribution of higher diffraction orders is seen as a kind of background, which disturbs the measurements. As discussed in Sect. 5.2 it is theoretically possible to suppress and enhance individual diffraction orders of a ZP by design. However, to produce a ZP with completely suppressed disturbing orders is a challenging task.

An alternative to avoid confusion by the higher diffraction order background is given by geometric considerations. In the following, two possibilities to reduce the background by higher diffraction orders is presented.

5.4.1. The diffracted wavefront - using apertures to select the collimated beam

One solution to suppress contributions of higher convergent and divergent orders of the ZP is to place the optic in a certain distance z along the optical axis to the ZP. To determine this distance z , the fundamental physics of a ZP has to be considered. A ZP is a rotationally symmetric grating with a radially increasing line density. With increasing radius r of the ZP also the diffraction angle increases. At the edge of the ZP the angle between incident and diffracted light is largest while at the center of the ZP the angle between the incident beam and the diffracted X-rays is zero. For the estimates given here we take only neighboring orders to the collimated beam of order $m = 1$ into account that are the diffraction angle of the convergent order $m = 2$ and the diffraction angle of the divergent order $m = 0$.

Fig. 21a schematically demonstrates the set-up for an obstructed ZP with an outer radius r_a and an inner radius r_i . For $r < r_i$ the ZP is masked and the illuminated area of the ZP is a ring with width $\Delta r = r_a - r_i$. The ZP ring diffracts the divergent beam. This results in a characteristic annular beam for each order. Fig. 21b shows ray tracing simulations at the distance z to the ZP considering the orders $m = 0, 1, 2$ with the collimated one in the middle.

For calculating the required width Δr of the annular collimated beam to separate the orders from each other the intercept theorem of similar triangles is used. The geometry is shown in Fig. 21a. For order $m = 2$ the distance $z_{m=2}$ is calculated with Eq. (24) and for order $m = 0$ $z_{m=0}$ is calculated with Eq. (25) respectively.

$$\frac{r_a}{r_i} = \frac{f}{f - z_{m=2}} \Rightarrow z_{m=2} = f \cdot \left(\frac{\Delta r}{r_a} \right) \quad (24)$$

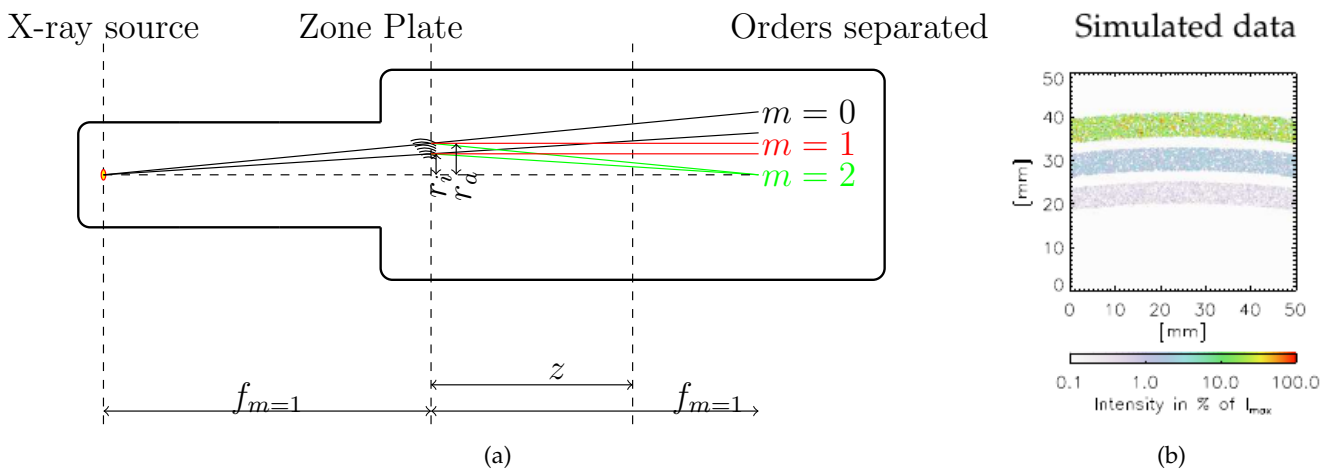


Figure 21: Geometric separation of grating orders. (a) A ZP with focal length $f_{m=1}$ diffracts the X-ray beam. The collimated annular beam (order $m = 1$) can be geometrically separated from the divergent beam ($m = 0$) and convergent beam ($m = 2$) at a distance z to the ZP. (b) Detector view at a distance z to the ZP based on ray tracing results. Annular beams are detectable and separated. The beam in the middle is the collimated beam of order $m = 1$.

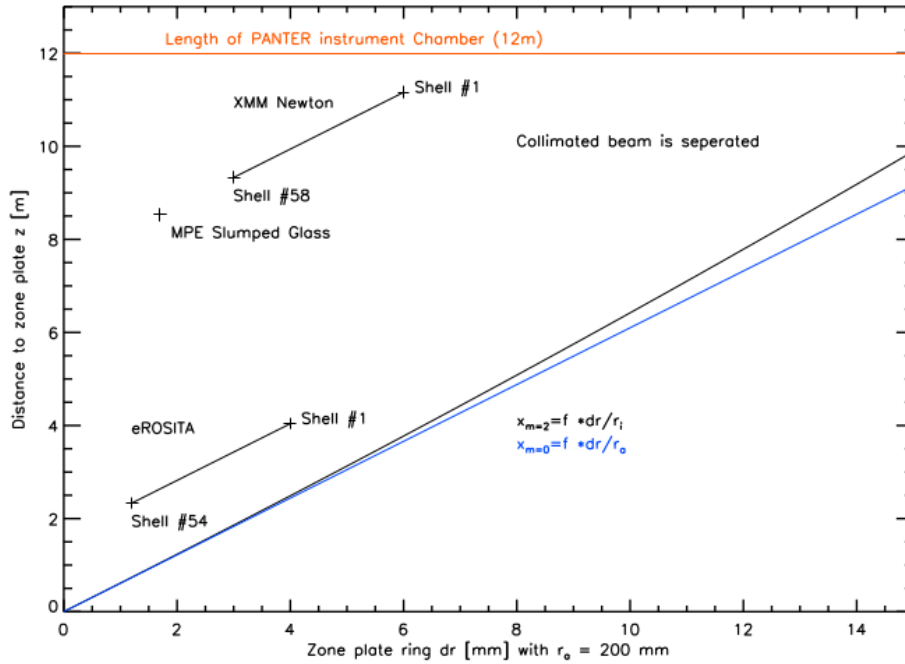


Figure 22: The distance z between the ZP and the Wolter optic depends on the ring width Δr of the ZP. In this graph the function $\Delta r(z)$ for a ZP with an outer radius $r_a = 200$ mm and focal length $f = 122$ m is shown. An increasing ZP ring width Δr increases the distance to the ZP where the collimated beam can be separated. As an example several X-ray optics such as XMM-Newton, eROSITA, and slumped glass optics of MPE with focal length f_{Mirror} are put into the graph at the proper distance. For the necessary ring width Δr the geometric area of the parabolic mirror part is calculated. This ring width results in a distance z to the ZP where the optics can be placed. Adding the focal length f_{Mirror} to the distance z it can be shown that all these optics can be analyzed with a collimated beam in the PANTER X-ray test facility.

$$\frac{r_a}{r_i} = \frac{f + z_{m=0}}{f} \Rightarrow z_{m=0} = f \cdot \left(\frac{\Delta r}{r_i}\right) \quad (25)$$

To estimate the distance z as a function of the ring width Δr for the dimensions of the PANTER X-ray test facility the focal length $f_{m=1}$ is substituted with $f_{m=1} = 122$ m (i.e. the distance to the X-ray source) and the outer ZP radius is substituted with $r_a = 200$ mm, the largest reasonable radius according to Sect. 5.3. Fig. 22 shows calculated values for the distance z to the ZP as a function of the effectively usable ring width Δr . For a larger radial beam size Δr the distance between ZPC and the X-ray optic z has to be increased. As an example typical X-ray optics with the corresponding projected shell sizes. E.g. the eROSITA mirror shells have a projected radial shell size from 1.5 mm to 4 mm. To measure such a shell, a collimated radial beam size of a view millimeters is necessary. Hence, the optics has to be mounted at least at a distance of 1.5 m to the ZP.

To measure an ATHENA module requires a radial beam size of 35 mm, as discussed in Sect. 3.2.2. Hence, the SPO needs to be placed in this configuration in a distance of $x = 21.35$ m. In the default PANTER configuration, with an instrument chamber length of 12 m, this is not possible. However, based on the modular upgrade of the PANTER facility (extra 13 m length) such a set-up can be realized. Alternatively, a ZP with a shorter focal length of e.g. 100 m would provide the possibility to measure an ATHENA optic module completely with the default set-up.

5.4.2. Imaging multiple point sources - angular distance in the detector plane

A second solution to separate non collimated order effects is based on the order separation in the detector plane. It is therefore necessary to approximate the distance d between the point image in the detector plane and the out of focus

contribution of higher orders. For an optic with focal length f the image distance b can be calculated by using the thin lens equation (5) which depends on the object distance g .

For a ZP an appropriate object distance g_m for each order m exists. The object width for the collimated order $m = 1$ is $g_{m=1} = \infty$ and $b = f$. For orders $m \leq 0$ the beam is divergent and $b > f$ while for $m \geq 2$ the beam is convergent and $b < f$.

Using a ZP as collimator leads to m focal planes with a point image and out of focus contributions in each focal plane. Here is estimated the distance of the point image and the out of focus contributions in the focal plane on the detector for order $m = 1$.

As discussed in Sect. 3.2 X-ray telescope optics use reflective mirrors in the Wolter type 1 configuration to focus X-rays and the angle between incident and reflected ray is constant. Therefore, the separation of the point image depends on the Wolter optic that will be analyzed and the angle δ between the incident rays.

For a mirror with focal length f_{Mirror} and radius r_{Mirror} the light is reflected with an angle α with $\tan \alpha = r_{Mirror} / f_{Mirror}$. The angle δ between the collimated and direct beam leads to a distance d between the focal point (of the collimated beam) and the out of focus beam (of the divergent beam $m = 0$) in the detector plane (see Fig. 23a). The angle δ is given by $\tan \delta = r_{ZP} / f_{ZP}$ with the radius r_{ZP} and the focal length of the ZP f_{ZP} .

Using trigonometry it can be shown that:

$$\frac{r_{Mirror} - d}{f_{Mirror}} = \tan(\alpha - \delta) \quad (26)$$

and using the small angle approximation that $\tan(\alpha - \delta) \approx \alpha - \delta$ which is fulfilled here Eq. (26) transforms to:

$$\frac{d}{f_{Mirror}} = \frac{r_{ZP}}{f_{ZP}} \quad (27)$$

To estimate the distance d relative to the mirror focal length f_{Mirror} for the dimensions of the PANTER X-ray test facility the focal length f_{ZP} is substituted with $f_{ZP} = 122$ m (i.e. the length of the PANTER X-ray beam line) and the ZP radius is substituted with $r_{ZP} = 200$ mm. For these dimensions the distance d between the in focus point image and the out of focus contributions in the focal plane relative to the mirror focal length f_{Mirror} is $d / f_{Mirror} \approx 340$ arc sec. This is orders of magnitudes larger, than the resolution required for ATHENA.

A simulation with such a configuration is done using the ZEMAX ray tracing program and shown in Fig. 23b. As a focusing Wolter optic a slumped glass unit [41] is used. Such an optic was measured in the X-ray test facility PANTER in 2013 with the divergent beam. The simulated data are based on a surface measurement, also obtained in 2013. X-ray measurements and simulated data showed good agreement.

As the resolution of this optic (HEW ≈ 70 arc sec) is not comparable to the resolution required for ATHENA optics, a larger outer ZP radius of 375 mm, and hence $d / f_{Mirror} \approx 640$ arc sec, is used for the simulations. Such a large ZP radius is not suitable for the ATHENA configuration, as chromatic aberrations would cause angular aberrations in the range of several 0.1 arc sec. However, it is possible to demonstrate the separation of diffraction order in the detector plane with the available data and simulations. With the larger ZP radius the resolution of the optic is ten times smaller than the distance of higher order contributions. A separation of the point images is possible by eye in Fig. 23b.

This configuration enables a simple set-up to measure ATHENA type X-ray optics. An alignment of the masks with respect to the ZP and the X-ray optic is not necessary. This makes this solution easier than the set-up presented in Sect. 5.4.1. Additionally, this set-up enables to measure with the available PANTER beam path, which will be discussed in the next section. However, the optic needs to fulfill the resolution requirements as needed for ATHENA (5 arc sec), in order to separate the point image contributions in the detector plane.

6. Design of the Zone Plate Collimator

To realize a ZP, which primarily can be used as a collimator for the PANTER X-ray test facility, we present in the following a feasible design. Based on the discussions on X-ray optics in section 3 and ZP optics in section 5 we have determined three requirements for the ZPC:

- The optical requirements for the angular resolution should be significantly better than the angular resolution required for ATHENA.

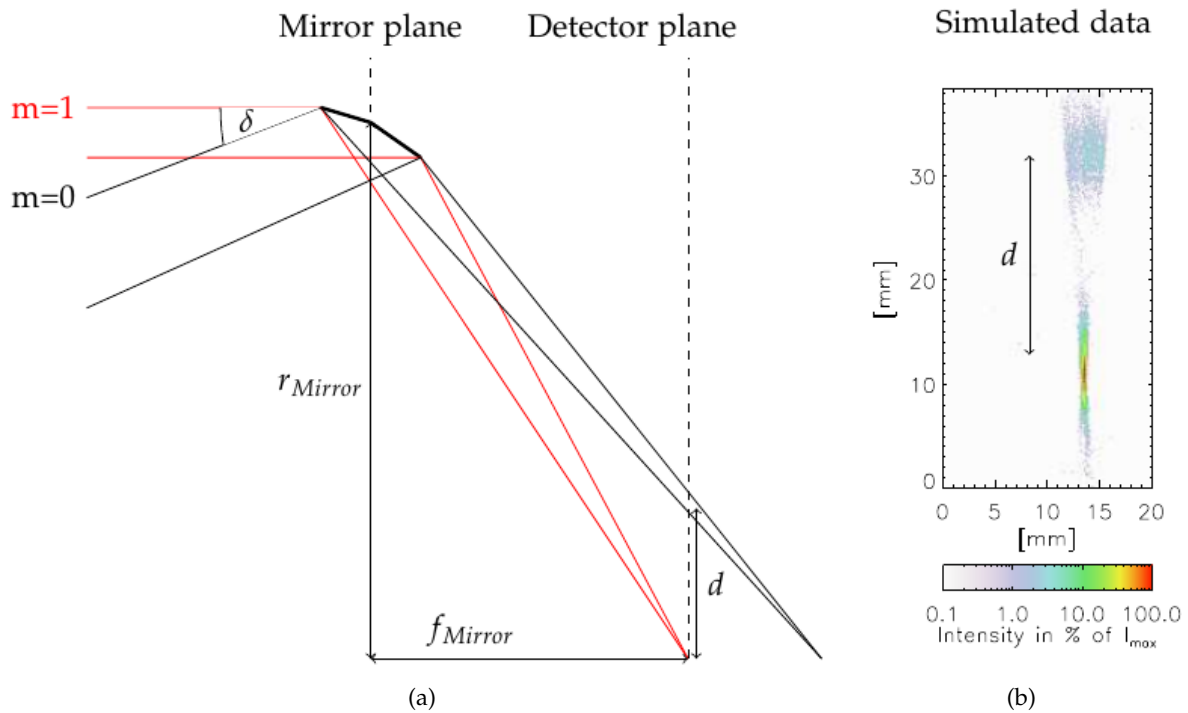


Figure 23: Geometric separation of diffraction orders in the detector plane. (a) Schematic of the light path for the collimated beam ($m = 1$) and the direct beam ($m = 0$). The beams are focused by using a Wolter type optic. The angle δ between the two incident beams yields a separation in the detector plane d . (b) Point images in the detector plane: For each ZP order a point image exists. The size of the focused point image in the detector plane depends on the resolution of the Wolter optic and the focus position. In the y-axis the size of the point image is extended due to figure errors of the mirror. In the x-axis the size of the point image mainly depends on focal length errors. For the collimated beam the point image is in focus while for all other orders out of focus contributions are present. Presented are here the point images of order $m = 0$ and order $m = 1$. For the simulations a ZP with radius $r_{ZP} = 375$ mm and focal length $f_{ZP} = 122$ m is assumed. For the focusing Wolter optic a slumped glass unit[41] is used. For this configuration the point image d and the out of focus contribution is separated. 3 m

- The area of the collimated beam should be comparable to the aperture of a SPO module.
- A low background contribution due to higher diffraction orders requires a large ZP radius is needed.

Theoretically, all these three requirements need a ZP radius as large as possible. Practically, the radius of the ZPC is limited by ZP aberrations (see section 5), by the set-up constraints of the PANTER X-ray test facility, and by the fabrication process. In this section we examine the fabrication process and determine the extent to which an appropriate ZPC can be realized.

As elaborated in section 5, a ZP is a three-dimensional rotationally symmetric diffraction grating. The change of the optical light path is defined by the geometry of the zone rings, basically the top view of the ZP. The efficiency of ZP depends on the height of the phase shifting structure, basically the side view of the ZP. With the top and the side view, the three-dimensional diffraction grating of the ZP is defined.

The fabrication of the ZP has been taken over by the IAP at the University of Jena under the direction of Ernst-Bernhard Kley. In collaboration with the IAP we developed a design for the ZPC that meets the requirements and that is feasible. In this section is defined the design, which can be seen as the top view of the ZP (see Sect. 6.1). The essential process steps to realize the ZP, described in Sect. 6.2, give basically the side view of the ZP.

6.1. Design of the ZP

In order to specify the design of the ZP, the basic ZP equation for large zone numbers n [1, 21]

$$2r_n \Delta r_n = \lambda f \quad (28)$$

is used. This equation defines the relation of the aperture radius r_n of a ZP to the width of the outermost zone Δr_n , the focal length f , and the wavelength λ .

As the ZP design strongly depends on energy, this parameter is discussed first. Although the requirements for the ATHENA optics are defined at 1 keV, the ZP design is optimized for an energy of $E = 1.49$ keV ($\lambda = 0.834$ nm), the Al-K $_{\alpha}$ emission line.

For the ZPC set up at PANTER the use of a fluorescence line has the advantage that the X-ray source provides a high brilliance. The available Multi-Target electron impact X-ray source provides for the Al-K $_{\alpha}$ emission line a small spectral bandwidth, a high flux, and a small spot size. Especially its spectral bandwidth is essential, as therefore chromatic aberrations of the ZP are reduced (see Sect. 5.3). A monochromator would also enable measurements with a small bandwidth, however, at the expense of the flux and a smaller spot size. Hence, it was decided to optimize the ZP design for the Al-K $_{\alpha}$ emission line. The optical parameters are, in what follows, optimized for this energy.

The angular HEW of the ZPC can be calculated with $\delta_{HEW} = \zeta \Delta r_n / f$ [3], where $\zeta = 0.535$ is used for HEW conversion. In order to obtain a large r_n and a good angular resolution δ_{HEW} , it follows from the HEW relation and Eq. (28) that Δr_n has to become small while f has to become large. Specifically, this means for the PANTER X-ray test facility that the ZPC has to be designed for a focal length $f = 122.292$ m, i.e. making use of the complete length of the PANTER vacuum tube.

As a final point in the design the narrowest structure Δr_n needs to be defined. This is essentially given by the fabrication technique. The possibilities using lithographic processes of the semiconductor industry are almost unlimited. Theoretically, the ambitious goal of a ZP with $\Delta r_n = 15$ nm can be adapted [1]. A corresponding ZP would have a diameter of 6.8 m. Besides the technical difficulties to produce such a ZP, chromatic aberrations of the PANTER X-ray source would affect the resolution of such a ZP significantly. The finite bandwidth of the Al-K $_{\alpha}$ emission line of 0.49 eV [18] would cause an error of 1.89 arc sec.

As elaborated in Sect. 5.3 an outer ZP radius of 20 cm is useful if it is required that chromatic aberrations have to be less than 0.1 arc sec. The smallest structure then has a size of $\Delta r_n = 252$ nm, which can be realized using e-beam lithography.

When using e-beam lithography, there are various possibilities for the actual production. Well known process steps as well as the use of standard 4 inch and 6 inch wafer kept the ZP production in cost and time at a reasonable level. Taking into account that the wafer edge serves as a support structure, ZP areas with a radius of 2.5 cm or 5 cm, respectively, can be realized. Specifically, two designs are shown schematically in Fig. 24. The most important parameters for both designs are summarized in Table 5.

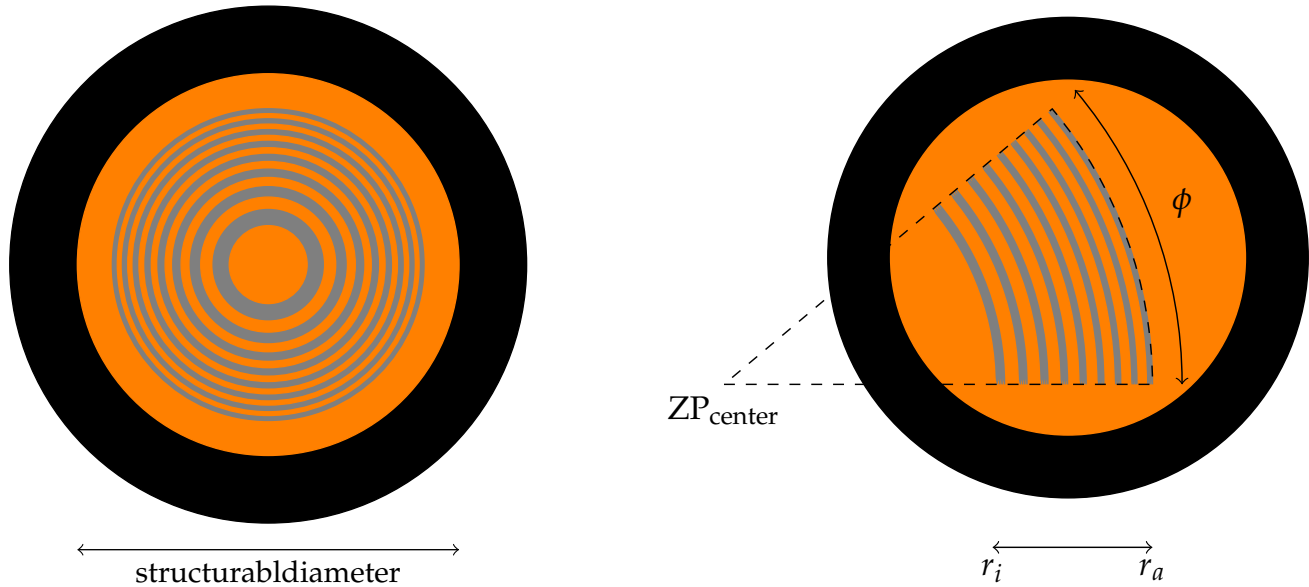
Originally a 4'' central ZP was fabricated as a proof of principle (see Fig. 24a).

From the experiences again with the 4 inch design ZP, and especially that the efficiency is significantly influenced by the fabrication, a design based on a 6 inch wafer has been defined, which in the following is called the 6 inch design ZP (see Fig. 24b).

The 6 inch wafer provides a significantly larger area. Additionally, the design is optimized to reduce background contribution by higher diffraction orders, as discussed in Sect. 5.4. The segmented design, as shown in Fig. 24b, allows an outer ZP radius of 20 cm. This ZP is designed with a space to period ratio $s : P = 1 : 2$ in order to optimize the first order efficiency and in order to maximize the fabrication tolerances (see Sect. 5.2.2).

6.2. Fabrication process of the ZPC

In the previous section the ZP design is given in two dimensions. In order to get a diffractive optic, this design has to be realized in the third dimension. An obvious problem is that a freestanding structure is not feasible. Consequently, the structure has to be appropriately supported. A further issue is that the high aspect ratios required are challenging to fabricate. As discussed in Sect. 5.2, the aspect ratio increases with ZP radius. However, the aspect ratio can be reduced by choosing a suitable material.



(a) The 4 inch design ZP. The ZP center coincides with the wafer center.

(b) The 6 inch design ZP. The ZP center is outside of the wafer. The ZP is realized as a segment with azimuthal length ϕ and radial length $r_a - r_i$.

Figure 24: Schematics of the realized ZP designs. The phase shifting structure (gray) is realized on a carrier film of Pwe (orange). A silicon ring (black) holds the Pwe carrier film.

Table 5: Realized and proposed zone plates.

ZP name	Realized	Proposed
Wafer size	4 inch	6 inch
Support structure thickness	Pwe 7.65 μm	Pwe 22.5 μm
transmission	37.1 %	5.42 %
Phase shift material thickness	Pwe 2.35 μm	W 0.422 μm
s:P	0.547	0.5
m=1 efficiency of grating bars	31.2 %	20 %
m=1 net efficiency of grating structure	31.2 %	20 %
m=0 efficiency of grating bars	10.3 %	10 %
m=0 net efficiency of grating structure	10.3 %	10 %
r_{in}	0 mm	125.28 mm
r_{out}	25 mm	200 mm
$\Delta\phi$	360°	25.5547°
diffraction limited resolution	3.68 milli arc sec	0.46 milli arc sec
theoretic first order efficiency m=1	11.6 %	1.02 %
theoretic first order efficiency m=0	3.82 %	0.737 %

The problem of a freestanding structure is thus solved by means of a carrier film⁷. A suitable carrier film has to have certain properties such as vacuum compatibility and a low outgassing rate. Among all the properties two are essential for the collimator set-up. The carrier film must provide enough stability and it must not be opaque to X-rays at 1.49 keV. From the second requirement it follows that materials with a low Z are most suitable, because they generally have a smaller absorption coefficient β . Consequently, the absorption of X-rays by the material is low.

⁷ Alternatively, a suitable system of support grids can give enough stability. However, the optimization of such a support grid requires a great effort, which was beyond the scope of this work.

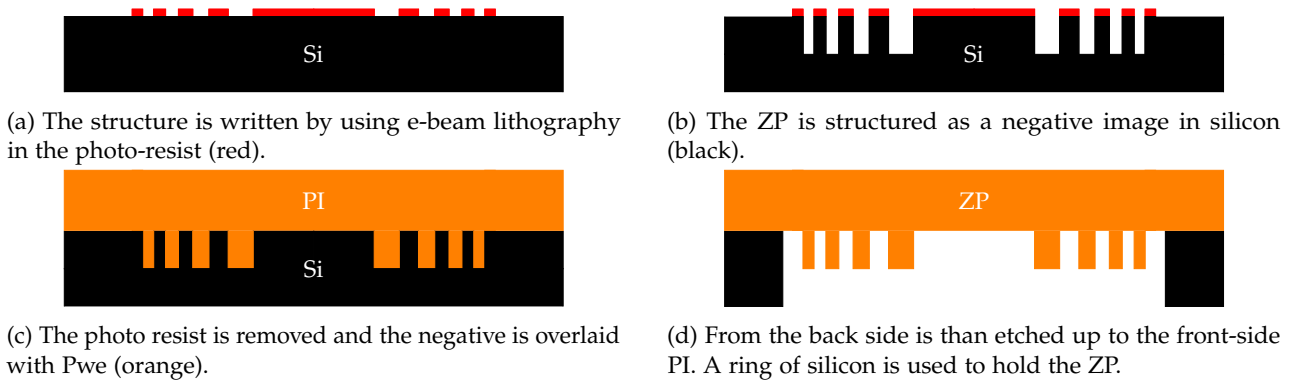


Figure 25: Fabrication process of the 4 inch design ZP.

Furthermore, the carrier film must be as thin as possible to provide a high transmissivity. Ultimately, however, the thickness of the carrier film is determined primarily specified by its stability.

The material of choice for the carrier film is PI. This carrier film material is characterized by its slight tension and is therefore a taut, yet tear-resistant membrane. Specifically DuPont type PI-2525 was used. The corresponding thickness of the PI and the transmissions for the two ZP designs are summarized in Table 5.

In addition, the Pwe carrier film provides sufficient tensile strength and stability during the handling, when evacuating, and when measuring the 4 inch design ZP. Due to these positive characteristics, the 6 inch design ZP uses also a carrier film made of PI. The higher absorption of the 6 inch design ZP carrier film compared to the 4 inch design ZP is taken into account as it can be compensated in principle by a higher source flux or longer exposure times.

The actual phase shifting structure of the ZP is fabricated on top of the carrier film or is embedded in the carrier film, depending on the ZP design. From the theoretical efficiency calculations of a ZP, discussed in Sect. 5.2 and shown in Fig. 16, different materials can be selected for the phase shifting structure. As discussed, the diffraction efficiency in general decreases with increasing atomic number Z . However, some materials are more suitable in order to achieve a high first order efficiency than others. Steps in the first order intensity are due to photoelectric absorption by K, L, or M shell electrons. Additionally, the aspect ratio has to be considered as limiting factor for the fabrication. The outer radius, and thus the smallest structure Δr_n , of the ZP and its optimal height as a phase shifting structure $z_{Profile}$ are determining factors for the aspect ratio.

Accordingly, for the 4 inch design ZP the smallest structure is $\Delta r_n = 2.04 \mu\text{m}$. This enables to use Pwe as the phase shifting material. The optimal profile height is $z_{Profile} = 2.35 \mu\text{m}$ and a resulting maximum aspect ratio of 1.15 is feasible. The significant advantage is that the carrier film and the phase shifting structure are made of the same material and that PI, a low Z material, enabling a high first order diffraction efficiency of 31.2% for the phase shifting structure.

For the 6 inch design ZP the fabrication becomes more challenging, as the smallest structure is $\Delta r_n = 0.253 \mu\text{m}$, which is much smaller than that in the 4 inch design ZP. Hence, a different material for the phase shifting structure is needed as Pwe would require extreme aspect ratios. For the 6 inch design ZP tungsten was used, as it provides a high first order diffraction efficiency of 21.8% for a high Z material and the IAP has a profound process experience in working with tungsten. To maximize the first order diffraction efficiency an optimal profile height of $z_{Profile} = 0.422 \mu\text{m}$ is needed and thus, the aspect ratio is maximal 1.67 which is feasible to fabricate.

The process steps for the 4 inch design ZP are shown schematically in Fig. 25. The structure is written by using e-beam lithography in the photo-resist (see Fig. 25a). Then, the ZP is structured as a negative image in silicon (Si) (see Fig. 25b). The photo resist is removed and the negative is overlaid with Pwe (see Fig. 25c). From the back side is then etched up to the front-side PI. The 4 inch design ZP profile, shown schematically in Fig. 25d, is held by a support ring of silicon.

For the 6 inch design ZP the process, shown schematically in Fig. 26, is as follows: Basic for the ZP is a Si wafer with a 80 nm Cr layer (green), a 422 nm W layer (blue), another 80 nm Cr layer, and the photo-resist SU-8 (red). The structure is written by using e-beam lithography in the photo-resist (see Fig. 26a). The structure is then etched positive. The Cr layer serves as an etch stop (see Fig. 26b). Then, the photo-resist and the Cr layer are removed and the structure is overlaid with Pwe (see Fig. 26c). From the back side is then etched the Si up to the phase shifting structure. The 6 inch design ZP profile, schematically shown in Fig. 26d, is held by a support ring of silicon.

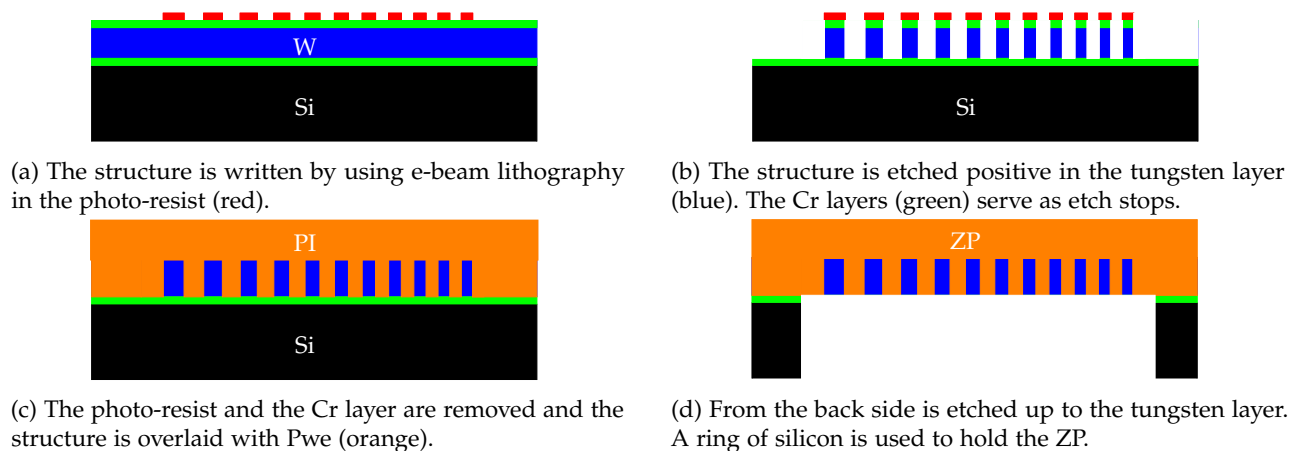


Figure 26: Fabrication process of the 6 inch design ZP. Basic for the ZP is a Si wafer with a 80 nm Cr layer (green), a 422 nm W layer (blue), another 80 nm Cr layer, and the photo-resist SU-8 (red)

7. Summary

In this report we have collected all the information that is necessary to be able to design and fabricate a zone plate optic that can provide a collimated X-ray beam (i.e. divergence $< 0.1''$) that is large enough to fully illuminate an Athena type mirror module at an energy of 1.49 keV (Al- K_{α}). The final design of an optimised zoneplate produced on a 6 inch wafer is given in the section 6.

Such a precise collimator optic will be important to help qualify and characterise the ATHENA optics during their development phase as well as during the production phase. Reports of tests using the a fabricated and tested Zoneplate collimator on Athena optics will be given in future reports as part of this AHEAD work package 8.2.

References

- [1] D. Attwood. *Soft X-Rays and Extreme Ultraviolet Radiation: Principles and Applications*. Cambridge University Press, 2007. ISBN: 9780521029971. URL: <https://books.google.de/books?id=c1AANTKBStcC>.
- [2] M Born and E Wolf. *Principles of Optics*. 7th ed. Cambridge University Press, 1999.
- [3] Christoph Braig et al. "Resolution limits of transmission optics for x-ray astronomy". In: *Proc. SPIE* 8443, 844341 (2012). DOI: 10.1117/12.925542. URL: <http://dx.doi.org/10.1117/12.925542>.
- [4] C. J. Burrows, R. Burg, and R. Giacconi. "Optimal grazing incidence optics and its application to wide-field X-ray imaging". In: *ApJ* 392 (June 1992), pp. 760–765. DOI: 10.1086/171479.
- [5] W. Cash et al. "Laboratory detection of X-ray fringes with a grazing-incidence interferometer". In: *Nature* 407 (Sept. 2000), pp. 160–162. DOI: 10.1038/407160a.
- [6] Kai-Wing Chan et al. "Aligning, bonding, and testing mirrors for lightweight x-ray telescopes". In: *Proc. SPIE* 9603, 96030Z (2015). DOI: 10.1117/12.2187016. URL: <http://dx.doi.org/10.1117/12.2187016>.
- [7] Weilun Chao et al. "Soft X-ray microscopy at a spatial resolution better than 15 nm". In: *Nature* 435.7046 (June 2005), pp. 1210–1213. ISSN: 0028-0836. DOI: 10.1038/nature03719. URL: <http://dx.doi.org/10.1038/nature03719>.
- [8] William W. Craig et al. "Fabrication of the NuSTAR flight optics". In: *Proc. SPIE* 8147, 81470H (2011). DOI: 10.1117/12.895278. URL: <http://dx.doi.org/10.1117/12.895278>.
- [9] A. J. Fresnel. "Calcul de l'intensité de la lumière au centre de l'ombre d'un écran et d'une ouverture circulaires éclairés par un point radieux". In: *Œuvres Complètes d'Augustin Fresnel, Imprimerie Impériale* (1866).
- [10] Michael Freyberg et al. "Potential of the PANTER x-ray test facility for calibration of instrumentation for XEUS". In: *Proc. SPIE* 6266, 62663H (2006). DOI: 10.1117/12.673300. URL: <http://dx.doi.org/10.1117/12.673300>.
- [11] Fiona A. Harrison et al. "The Nuclear Spectroscopic Telescope Array (NuSTAR) High-energy X-Ray Mission". In: *The Astrophysical Journal* 770.2 (2013), p. 103. URL: <http://stacks.iop.org/0004-637X/770/i=2/a=103>.
- [12] B.L. Henke, E.M. Gullikson, and J.C. Davis. "X-Ray Interactions: Photoabsorption, Scattering, Transmission, and Reflection at E = 50-30,000 eV, Z = 1-92". In: *Atomic Data and Nuclear Data Tables* 54.2 (1993), pp. 181–342. ISSN: 0092-640X. DOI: 10.1006/adnd.1993.1013. URL: <http://www.sciencedirect.com/science/article/pii/S0092640X83710132>.
- [13] Malcolm Howells et al. *Principles and Applications of Zone Plate X-Ray Microscopes*. English. Ed. by Peter W. Hawkes and John C. H. Spence. Springer New York, 2007, pp. 835–926. ISBN: 978-0-387-25296-4. DOI: 10.1007/978-0-387-49762-4_13. URL: http://dx.doi.org/10.1007/978-0-387-49762-4_13.
- [14] F. Jansen et al. "XMM-Newton observatory. I. The spacecraft and operations". In: *A&A* 365 (Jan. 2001), pp. L1–L6. DOI: 10.1051/0004-6361:20000036.
- [15] L. Kipp et al. "Sharper images by focusing soft X-rays with photon sieves". In: *Nature* 414 (Nov. 2001), pp. 184–188. DOI: 10.1038/35102526.
- [16] Janos Kirz. "Phase zone plates for x rays and the extreme uv". In: *J. Opt. Soc. Am.* 64.3 (Mar. 1974), pp. 301–309. DOI: 10.1364/JOSA.64.000301. URL: <http://www.opticsinfobase.org/abstract.cfm?URI=josa-64-3-301>.
- [17] G. Krämer et al. "Analysis and interpretation of soft X-ray photographs of coronal active regions taken with Fresnel zone plates". English. In: *Solar Physics* 57.2 (1978), pp. 345–367. ISSN: 0038-0938. DOI: 10.1007/BF00160108. URL: <http://dx.doi.org/10.1007/BF00160108>.
- [18] M. O. Krause and J. H. Oliver. "Natural widths of atomic K and L levels, K α X-ray lines and several KLL Auger lines". In: *Journal of Physical and Chemical Reference Data* 8 (Apr. 1979), pp. 329–338. DOI: 10.1063/1.555595.
- [19] J. Krizmanic et al. "Phase Fresnel lens development for X-ray and gamma-ray Astronomy". In: *Proc. 31st ICRC, Lodz* (2009).
- [20] D. Martínez-Galarce et al. "Multisegmented, multilayer-coated mirrors for the Solar Ultraviolet Imager". In: *Optical Engineering* 52.9, 095102 (Sept. 2013), p. 095102. DOI: 10.1117/1.0E.52.9.095102.
- [21] A. G. Michette. *Optical systems for soft x-rays*. Plenum Press, New York, 1986.
- [22] K. Nandra et al. "The Hot and Energetic Universe: A White Paper presenting the science theme motivating the Athena+ mission". In: *ArXiv e-prints* (June 2013). arXiv: 1306.2307 [astro-ph.HE].
- [23] G. Pareschi et al. "IXO glass mirrors development in Europe". In: *Proc. SPIE* 8147, 81470L (2011). DOI: 10.1117/12.895303. URL: <http://dx.doi.org/10.1117/12.895303>.
- [24] Peter Predehl. "eROSITA". In: *Proc. SPIE* 8443, 84431R (2012). DOI: 10.1117/12.925843. URL: <http://dx.doi.org/10.1117/12.925843>.
- [25] J. W. Rayleigh. "Wave theory of light". In: *Encyclopedia Britannica, 9th ed.* 24 (1889), p. 421.

- [26] T. T. Saha. "Transverse ray aberrations of Wolter type 1 telescopes". In: *Grazing incidence optics*. Vol. 640. Proc. SPIE. Jan. 1986, pp. 10–19.
- [27] Timo T. Saha. "Transverse ray aberrations for paraboloid–hyperboloid telescopes". In: *Appl. Opt.* 24.12 (June 1985), pp. 1856–1863. DOI: 10.1364/AO.24.001856. URL: <http://ao.osa.org/abstract.cfm?URI=ao-24-12-1856>.
- [28] H. W. Schnopper et al. "Diffraction grating transmission efficiencies for XUV and soft X rays". In: *Appl. Opt.* 16 (Apr. 1977), pp. 1088–1091.
- [29] K. Schwarzschild. "Untersuchungen zur geometrischen Optik I," in: *Astronomische Mitteilungen der Universitaets-Sternwarte zu Goettingen* 9 (1905), p. 1.
- [30] M.J. Simpson and A.G. Michette. "Imaging Properties of Modified Fresnel Zone Plates". In: *Optica Acta: International Journal of Optics* 31.4 (1984), pp. 403–413. DOI: 10.1080/713821522. eprint: <http://www.tandfonline.com/doi/pdf/10.1080/713821522>. URL: <http://www.tandfonline.com/doi/abs/10.1080/713821522>.
- [31] A. Snigirev et al. "Focusing high-energy x rays by compound refractive lenses". In: *Appl. Opt.* 37.4 (Feb. 1998), pp. 653–662. DOI: 10.1364/AO.37.000653. URL: <http://ao.osa.org/abstract.cfm?URI=ao-37-4-653>.
- [32] D. Spiga et al. "An expanded x-ray beam facility (BEaTriX) to test the modular elements of the ATHENA optics". In: *Proc. SPIE* 9144, 91445I (2014). DOI: 10.1117/12.2057358. URL: <http://dx.doi.org/10.1117/12.2057358>.
- [33] J. Trümper. "Der Röntgensatellit ROSAT". In: *Physik Journal* 46.5 (1990), pp. 137–143. ISSN: 1521-3722. DOI: 10.1002/phb1.19900460502. URL: <http://dx.doi.org/10.1002/phb1.19900460502>.
- [34] L. P. VanSpeybroeck and R. C. Chase. "Design Parameters of Paraboloid-Hyperboloid Telescopes for X-ray Astronomy". In: *Appl. Opt.* 11.2 (Feb. 1972), pp. 440–445. DOI: 10.1364/AO.11.000440. URL: <http://ao.osa.org/abstract.cfm?URI=ao-11-2-440>.
- [35] M. C. Weisskopf et al. "An Overview of the Performance and Scientific Results from the Chandra X-Ray Observatory". In: *Publications of the Astronomical Society of the Pacific* 114 (Jan. 2002), pp. 1–24. DOI: 10.1086/338108. eprint: astro-ph/0110308.
- [36] W. Werner. "Imaging properties of Wolter I type X-ray telescopes". In: *Appl. Opt.* 16 (Mar. 1977), pp. 764–773. DOI: 10.1364/AO.16.000764.
- [37] E. Wille et al. "Qualification of silicon pore optics". In: *Proc. SPIE* 9144, 91442H (July 2014). DOI: 10.1117/12.2055950.
- [38] R. Willingale et al. "The Hot and Energetic Universe: The Optical Design of the Athena+ Mirror". In: *ArXiv e-prints* (July 2013). arXiv: 1307.1709 [astro-ph.IM].
- [39] C. E. Winkler and D. Korsch. "Primary aberrations for grazing incidence". In: *Appl. Opt.* 16 (Sept. 1977), pp. 2464–2469. DOI: 10.1364/AO.16.002464.
- [40] Anita Winter et al. "Analysis of the optical surface properties in the indirect glass slumping". In: *Proc. SPIE* 9144, 914442 (2014). DOI: 10.1117/12.2056892. URL: <http://dx.doi.org/10.1117/12.2056892>.
- [41] Anita Winter et al. "Light-weight glass optics for segmented x-ray mirrors". In: *Proc. SPIE* 8450, 84502E (2012). DOI: 10.1117/12.925910. URL: <http://dx.doi.org/10.1117/12.925910>.
- [42] H. Wolter. "Verallgemeinerte Schwarzschildsche Spiegelsysteme streifender Reflexion als Optiken für Röntgenstrahlen". In: *Annalen der Physik* 445 (1952), pp. 286–295. DOI: 10.1002/andp.19524450410.
- [43] R. W. Wood. "Phase-reversed zone plates and diffraction telescopes". In: *Philos. Mag.* 45 (1898), pp. 511–522.
- [44] M. Young. "Zone Plates and Their Aberrations". In: *J. Opt. Soc. Am.* 62.8 (Aug. 1972), pp. 972–976. DOI: 10.1364/JOSA.62.000972. URL: <http://www.opticsinfobase.org/abstract.cfm?URI=josa-62-8-972>.
- [45] William W. Zhang et al. "Toward diffraction-limited lightweight x-ray optics for astronomy". In: *Proc. SPIE* 9603, 96030Q (2015). DOI: 10.1117/12.2187081. URL: <http://dx.doi.org/10.1117/12.2187081>.